

## Article

# Photocatalytic Degradation of Diclofenac by Nitrogen-Doped Carbon Quantum Dot-Graphitic Carbon Nitride (CNQD)

Huzaikha Awang<sup>1,2</sup>, Tim Peppel<sup>1,\*</sup> and Jennifer Strunk<sup>1,\*</sup>

<sup>1</sup> Department of Heterogeneous Photocatalysis, Leibniz Institute for Catalysis, Albert-Einstein-Str. 29a, 18059 Rostock, Germany

<sup>2</sup> Preparatory Centre for Science and Technology, Universiti Malaysia Sabah, Jalan UMS, Kota Kinabalu 88400, Sabah, Malaysia

\* Correspondence: tim.peppel@catalysis.de (T.P.); jennifer.strunk@catalysis.de (J.S.)

**Abstract:** In this study nitrogen-doped carbon quantum dots/graphitic carbon nitride nanosheet (CNQD) composites with different contents of nitrogen-doped carbon quantum dots (NCQDs; 2, 4, 6, and 8 wt%) were synthesized. The morphological, physicochemical, and photoelectrochemical properties were investigated using complementary methods such as scanning electron microscopy (SEM), powder X-ray diffraction (pXRD), X-ray photoelectron spectroscopy (XPS), Fourier transform infrared spectroscopy (FTIR), UV/Vis spectroscopy in diffuse reflectance (DRS), photoluminescence (PL), nitrogen physisorption (BET), photocurrent response, and electrochemical impedance spectroscopy (EIS). The photocatalytic activity of the synthesized materials was assessed during diclofenac (DCF) degradation in an aqueous solution under visible light irradiation. As a result, improved photocatalytic efficiency in DCF degradation was observed for all the CNQD composites compared with bulk graphitic carbon nitride (bCN) and nanosheet g-C<sub>3</sub>N<sub>4</sub> (CNS). The fastest DCF degradation was observed for the 6 wt% NCQD on the surface of CNS (CNQD-6), which removed 62% of DCF in 3 h, with an associated  $k$  value of  $5.41 \times 10^{-3} \text{ min}^{-1}$ . The performance test results confirmed the contribution of NCQDs to enhancing photocatalytic activity, leading to an improvement factor of 1.24 over bCN. The morphology of the CNS and the synergistic interaction between NCQDs and CNS were essential elements for enhancing photocatalytic activity. The photoelectrochemical data and photoluminescence analyses showed the efficient migration of photoexcited electrons from NCQDs to the CNS. The reduced charge recombination rates in CNQD photocatalysts might be due to the synergistic interaction between NCQDs and CNS and the unique up-conversion photoluminescence properties of NCQDs. Further investigations revealed that the photogenerated superoxide radicals ( $\bullet\text{O}_2^-$ ) predominated in the degradation of DCF, and this photocatalyst had good reusability and toxicity reduction abilities. This work provides insight into the effects of NCQDs on the CNS surface to enhance its potential to remove emerging organic pollutants from water and wastewater.

**Keywords:** nitrogen-doped carbon quantum dot (NCQD); graphitic carbon nitride (g-C<sub>3</sub>N<sub>4</sub>); photodegradation; diclofenac sodium (DCF); photocatalysis



**Citation:** Awang, H.; Peppel, T.; Strunk, J. Photocatalytic Degradation of Diclofenac by Nitrogen-Doped Carbon Quantum Dot-Graphitic Carbon Nitride (CNQD). *Catalysts* **2023**, *13*, 735. <https://doi.org/10.3390/catal13040735>

Academic Editors: Amr Fouda and Mohammed F. Hamza

Received: 27 February 2023

Revised: 30 March 2023

Accepted: 2 April 2023

Published: 13 April 2023



**Copyright:** © 2023 by the authors. Licensee MDPI, Basel, Switzerland. This article is an open access article distributed under the terms and conditions of the Creative Commons Attribution (CC BY) license (<https://creativecommons.org/licenses/by/4.0/>).

## 1. Introduction

Population expansion and modernization have increased the demand for pharmaceuticals and personal care products (PPCPs). The excessive discharge of PPCPs into wastewater has created a severe problem for the aquatic environment and wastewater treatment plants (WWTPs) [1]. It was reported that PPCPs contribute to the most significant sink in WWTPs [2–4]. Furthermore, it was reported that the conventional WWTPs method could not efficiently degrade the discharge of PPCPs due to their refractory nature [5,6]. Even though PPCPs are essential for human health and well-being, they expose consumers to a variety of chemical additives and organic pollutants, such as parabens, phthalates, bisphenol A (BPA), and diclofenac sodium (DCF), which is the basic element

of non-steroidal anti-inflammatory drugs (NSAIDs) [7–10]. The unavoidable exposure of humans to various chemicals in PPCPs has led to the high potential for health risks such as endocrine-disrupting effects [11–13], carcinogenic effects [14], premature births, growth limitations, gestational hypertension, abnormal sperm quality [11–13,15], and difficulties with anogenital distance in sexual development, allergies, asthma, and child behavior [14,16–18]. Besides these effects, the impact of PPCPs on marine organisms is also crucial and has become a current challenge in research [19].

In recent decades, a significant increase in DCF concentrations in wastewater has been reported, from a nanogram per liter to a microgram per liter [20]. Therefore, DCF has been added to the EU Water Framework Directive Watch List (Commission Implementing Decision 2015/495) [10,21]. The low elimination rates of DCF in wastewater occurred due to its weak biodegradability [22,23]. Currently, several identified methods, including photocatalytic degradation, have been employed to capture or degrade DCF [1,24–27], such as adsorption [23], ozonation [28], photoelectrocatalytic degradation [29], and bioremediation [30]. It was suggested that the organic contaminants in wastewater must be removed using highly consistent, ecologically friendly, and economical treatment procedures [27,31]. Photocatalytic degradation can be described as an ecologically friendly and economical treatment procedure because it can fully degrade resistant pollutants and mineralize organic pollutants into carbon dioxide and water using only a photocatalyst and light irradiation [32–36].

Graphitic carbon nitride ( $g\text{-C}_3\text{N}_4$ ) has recently gained popularity in photocatalytic degradation reactions to remove PPCPs from wastewater due to its good chemical and optical properties as a semiconductor, with a 2.7 eV band gap, low cost, and no ecotoxicity [24,37]. In addition,  $g\text{-C}_3\text{N}_4$  has outstanding thermal and chemical stabilities, tunable electronic band structures, and excellent visible light response activities [38–43]. Therefore, several studies have been carried out to use  $g\text{-C}_3\text{N}_4$ -based photocatalysts for DCF degradation, for example,  $g\text{-C}_3\text{N}_4/\text{BiVO}_4$  [29],  $\text{Ag}_3\text{PO}_4/g\text{-C}_3\text{N}_4$  [44], ruthenium-doped  $g\text{-C}_3\text{N}_4$  (CNRu) [45], and boron-doped  $g\text{-C}_3\text{N}_4$  [46]. However, to enhance their potential for practical application, it is crucial to address the small surface areas and high electron–hole recombination rates of  $g\text{-C}_3\text{N}_4$  [47].

Several studies have proposed using the surface integration method with carbon quantum dots (CQDs) to improve the high electron–hole recombination rate and broaden the light absorption region in  $g\text{-C}_3\text{N}_4$  [32,48–50]. CQDs are referred to as carbon dots (CDs), which are noted for their zero-dimensional (0D) structure, sub-ten-nanometer particle sizes, and predominant composition of carbon, nitrogen, and oxygen [51]. CQDs have become the most interesting of the nanocarbon family because of their remarkable ability to emit tunable high fluorescence over the visible spectrum, ability to donate and absorb electrons, high sensitivity, high solubility in water, biocompatibility, and ease of synthesis [51]. In addition, CQDs have been shown to act as electron reservoirs to capture photoexcited electrons, leading to higher charge separation efficiencies [52]. The heterogeneous doping of CQDs with atoms of nitrogen [52], palladium [53], sulfur [54], and phosphorous [55] has been demonstrated to be able to enhance photocatalytic performance. The majority of research has been focused on nitrogen-doped CQDs (NCQDs) because of their high quantum yields (QY), narrow band gap due to an increase in electron density, and longer absorption wavelengths [54]. NCQDs can be synthesized by using nitrogen-containing precursors such as urea [52,54,56,57] and ethylenediamine [58]. Several studies have been carried out to utilize the attractive properties of CQDs by coupling them with semiconductors such as CQD/ $\text{TiO}_2$  [58], CQD/ $\text{ZnO}$  [56], and NCQD/ $\text{PrFeO}_3$  [57]. However, the potential of harmful metal leaching during the photocatalytic process is the primary problem with these semiconductor composites [59].

NCQD/ $g\text{-C}_3\text{N}_4$  composites have been reported to have excellent efficiency in photocatalytic degradation, such as methylene blue (MB) degradation [52] and DCF degradation [24,50]. However, it should be noted that although the hybridization of NCQDs and  $g\text{-C}_3\text{N}_4$  have been reported, the synthesis method and morphological, physicochemical,

and photoelectrochemical properties of NCQD/g-C<sub>3</sub>N<sub>4</sub> composites still need more detailed research and differ from one study to another. To the best of our knowledge, there are still only few studies that investigate the effect of the photocatalysis of NCQDs/g-C<sub>3</sub>N<sub>4</sub> nanosheets on the photocatalytic degradation of DCF under visible light irradiation.

In this study, the hydrothermal synthesis method was used to synthesize NCQDs and couple them with nanosheet g-C<sub>3</sub>N<sub>4</sub> (CNS). The introduction of NCQDs did not affect the morphology and structure of CNS. The physicochemical and photoelectrochemical properties of CNQD composites were studied and showed a slight alteration compared with bCN and CNS, which affected the photocatalytic degradation of DCF. The underlying mechanism was investigated via scavenger tests, which are important to better understand the mechanism reactions in CNQD composites. In addition, toxicity reduction and reusability tests were performed to investigate the photostability of CNQD composites.

## 2. Results and Discussion

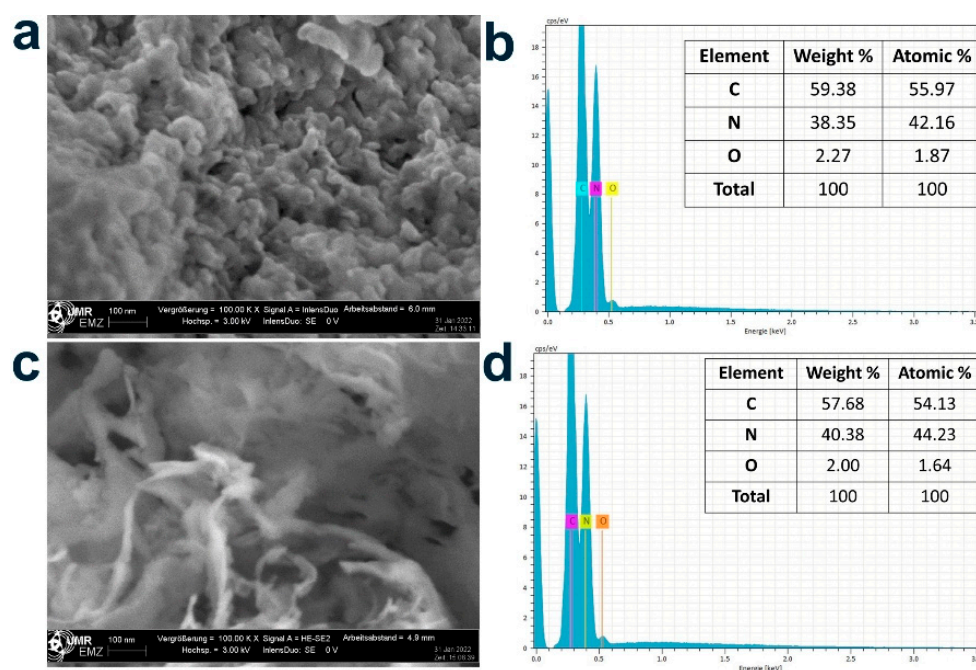
### 2.1. Characterization

Table 1 shows the elemental analysis results of bCN, CNS, NCQDs, and CNQD composites. NCQDs contained the following elements, in wt%: C 36.0, H 6.3, and N 14.7. bCN contained C 29.4, H 2.0, and N 55.9 (wt%), while CNS contained C 31.1, H 3.8, and N 59.3 (wt%). The weight percentage of the C elements in CNQD composites was slightly increased compared with pristine CNS, which indicates that NCQDs were successfully incorporated into the surface of CNS. An ideally layered g-C<sub>3</sub>N<sub>4</sub> has a 0.75 C/N molar ratio [60]. From Table 1, it can be inferred that the C/N atomic ratio in both bCN and CNS was 0.61. However, with the introduction of NCQDs, the C/N atomic ratio in the CNQD photocatalysts slightly increased to 0.62, 0.63, 0.63, and 0.65 for CNQD-2, CNQD-4, CNQD-6, and CNQD-8 photocatalysts, respectively. The increase in the C/N atomic ratio after the introduction of NCQDs is similar to the results of a previous study [61].

**Table 1.** Elemental analyses (C, H, and N) of bCN, CNS, NCQD, and CNQD composites.

Sample	C (wt%)	H (wt%)	N (wt%)	C/N Atomic Ratio
NCQD	36.0	6.3	14.7	2.85
bCN	29.4	2.0	55.9	0.61
CNS	31.1	3.8	59.3	0.61
CNQD-2	32.4	1.2	60.9	0.62
CNQD-4	32.1	1.4	59.5	0.63
CNQD-6	31.8	1.7	58.6	0.63
CNQD-8	31.4	1.6	56.8	0.65

The surface morphologies of bCN and CNS photocatalysts were investigated using SEM measurements (Figure 1). From Figure 1a, it can be seen that bCN mainly exhibits a spherical-like structure consisting of solid agglomerates, which is in agreement with previous studies [62]. In contrast, the CNS material in Figure 1c shows a chiffon-like curled wrinkle structure at the edges, indicating a decrease in the surface energy due to the successful delamination of bCN into a sheet-like structure [47]. Furthermore, the morphology of bCN significantly changed to a sheet-like structure after undergoing a second thermal polymerization process. This change proves that the polymerization process affects the microstructure of g-C<sub>3</sub>N<sub>4</sub> photocatalysts. As shown in the EA analysis results (Table 1), the total concentration of carbon, hydrogen, and nitrogen in bCN was 87.3%, and the remaining percentage of 12.7% could be assumed as the residual bulk oxygen content. However, the EA analysis results indicate a reduction in the oxygen content in CNS, which had only 5.8%. The EDX results of bCN and CNS in Figure 1b,d show that their weight percentages of near-surface oxygen were 2.3% and 2.0%, respectively. Therefore, oxygen depletion in CNS was confirmed with EA and EDX analyses.



**Figure 1.** SEM image (a) and EDX analysis results (b) of bCN; SEM image (c) and EDX analysis results (d) of CNS.

The surface morphologies, EDX, and elemental mapping of NCQDs were investigated using SEM (Figure 2). The SEM images of NCQDs in Figure 2a show the network-like shape of the particles. Tyndall effect investigations revealed a strong blue fluorescence emission in NCQD solutions under UV light irradiation, as shown in Figure 2b. The emission of blue fluorescence under UV light is one of the unique properties of NCQDs, and similar results were reported in previous studies [50]. The blue luminescence was ascribed to residual carboxyl groups (-COOH) and was later confirmed using FTIR and EA measurements. As shown in the EA analysis results (Table 1), NCQDs contained 36.0% C, 6.3% H, and 14.7% N, and the remaining 43.0% could be attributed to be the bulk oxygen content. The existence of oxygen in NCQDs was also confirmed by the EDX analysis results (Figure 2c), which revealed a near-surface oxygen weight percentage of about 15.4%. The surface passivation phenomenon enhances the stability and dispersibility of NCQDs, which can reduce the radiative combination of electron-hole pairs due to trapped electrons in the surface states and enhance the photocatalytic degradation rates [58]. The EDX analysis results in Figure 2c and elemental mapping in Figure 2d successfully validate the absence of impurities on NCQDs. The C content was derived from citric acid during the synthesis of NCQDs.

The surface morphologies of CNQD-6 photocatalysts were investigated using SEM, as shown in Figure 3. The morphology of CNQD-6 shows some degree of aggregation, which could have occurred during the NCQD and CNS coupling process. However, NCQDs were not observed, as the support contained the same elements.

Photographs of the as-prepared photocatalysts are shown in Figure 4. There is a significant change in color from bCN (Figure 4a) to CNS (Figure 4b). The bCN powder exhibits a brighter yellow color than CNS. The photographs of Figure 4c–f represent CNQD-2, CNQD-4, CNQD-6, and CNQD-8 photocatalysts, respectively. These photos clearly show that the soft yellow color of CNS became brownish black after introducing NCQDs, which gradually darkened with the increase in the weight percentage of NCQDs.

Powder X-ray diffraction (pXRD) patterns, as depicted in Figure 5, show the crystal phase structures and crystallinity of the synthesized photocatalysts. All the samples exhibited two distinctive  $g\text{-C}_3\text{N}_4$  diffraction reflexes (JCPDS Card No. 00-066-0813) located at  $2\theta = 13.2^\circ$  (100) and  $27.4^\circ$  (002), which are related to the interlayer stacking structure of the conjugated aromatic system and tri-s-triazine ring in-plane compression, respectively [63].

The two distinctive diffraction reflexes of bCN were located at  $2\theta = 13.2^\circ$  and  $27.48^\circ$ , while the reflexes of CNS were located at  $2\theta = 13.2^\circ$  and  $27.40^\circ$ . The same located reflexes indicate that the morphology evolution from bCN to CNS did not change the graphite-like phase structure. The slight shift in the 002 reflexes of CNS and bCN is attributed to the narrowing of interlayer spacing [24], which indicates a faster charge transfer rate to enhance photocatalytic performance [47,64]. In addition, the reduction in the 002 broad diffraction reflexes of CNS, compared with bCN, indicates that the crystallinity size of CNS slightly decreased. The CNS and CNQD photocatalysts exhibited similar XRD characteristic reflexes at  $2\theta = 13.2^\circ$  and  $27.40^\circ$ . The intensity of 002 diffraction reflexes of CNQD composites slightly changed compared with CNS, indicating changes in the crystal size of CNQD composites. The same characteristic reflexes demonstrates that the graphite-like phase structure of CNS did not change with the introduction of NCQDs, which is in line with the SEM analysis, as depicted in Figure 3. The structural integrity of CNS remained intact when loaded with NCQDs, similar to the results reported by previous studies [47,52].

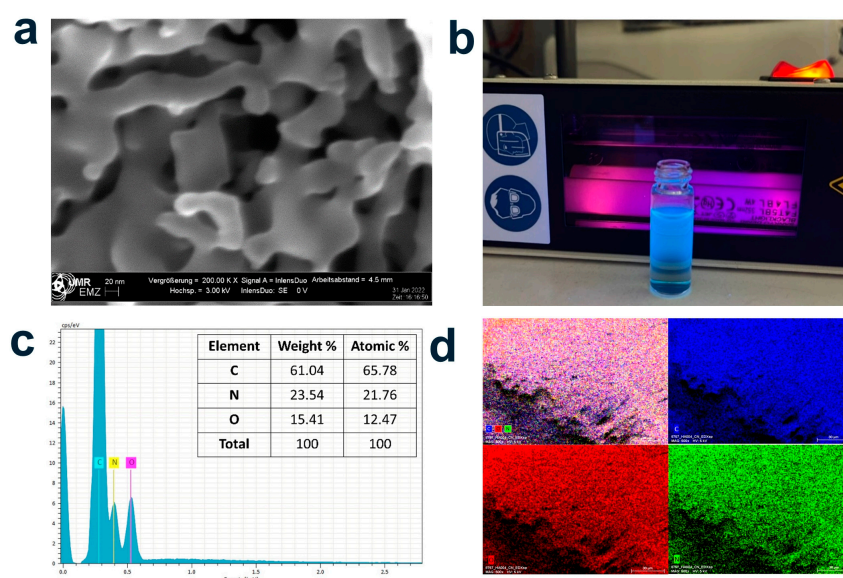


**Figure 2.** SEM image (a), Tyndall effect (b), EDX analysis (c), and EDX mapping for carbon C, N, and O of NCQDs (d).

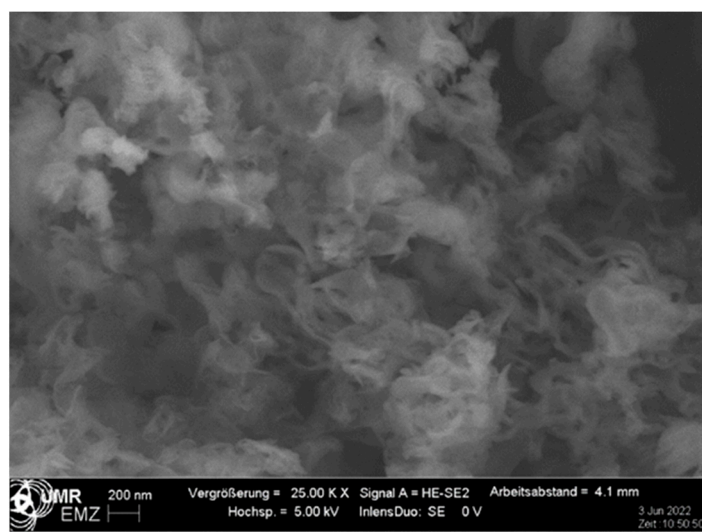


**Figure 3.** SEM image of 6 wt% NCQD/CNS (CNQD-6).

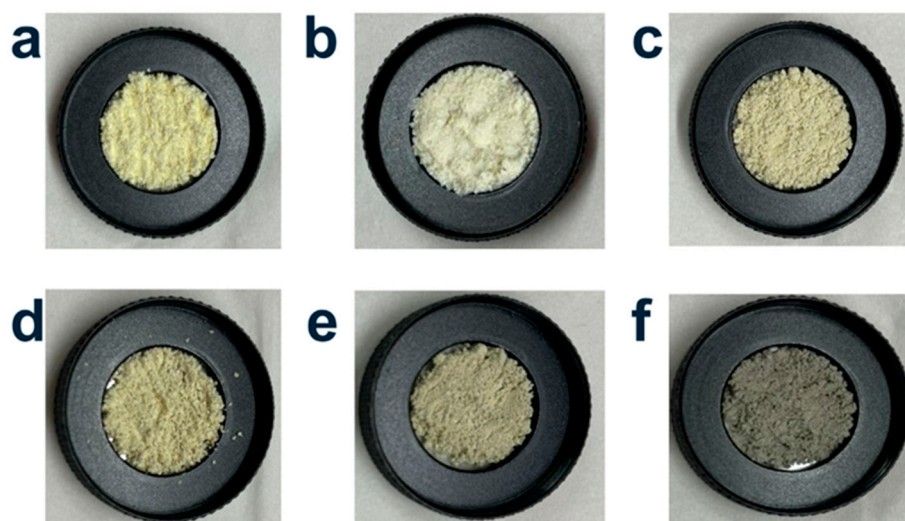


Figure 4. Photos of the (a) bCN, (b) CNS, and (c–f) CNQD photocatalysts.

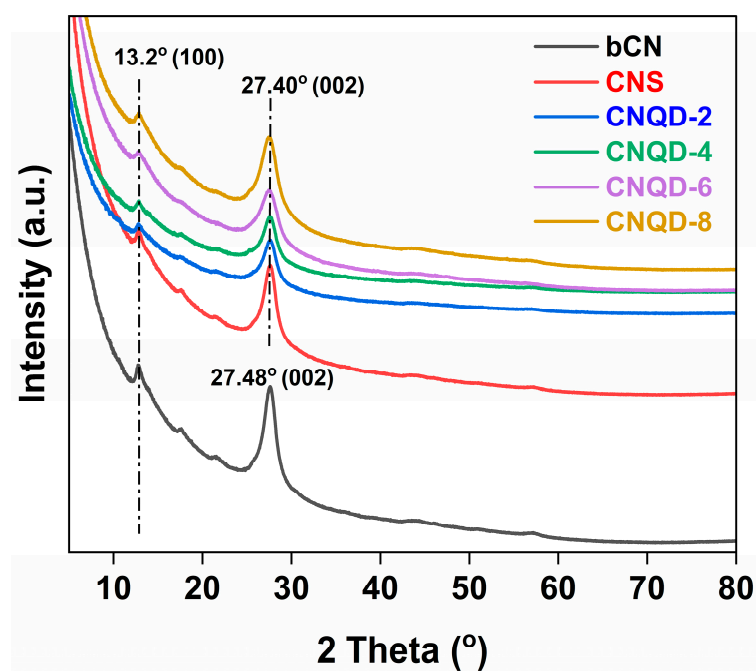


Figure 5. XRD patterns of bCN, CNS, and CNQD photocatalysts.

FTIR measurements were performed to evaluate the residual functional groups of NCQD, CNS, and CNQD photocatalysts, as shown in Figure 6. The CNS and CNQD photocatalysts exhibited similar  $g\text{-C}_3\text{N}_4$  stretching and bending vibrations at  $3000\text{--}3500\text{ cm}^{-1}$ ,  $1000\text{--}1800\text{ cm}^{-1}$ , and  $812\text{ cm}^{-1}$ , which are attributed to the vibrational modes of N–H and O–H groups, C–N and C=N heterocycles and tri-s-triazine, respectively [24,37]. The full FTIR spectra of CNS and CNQD composites (Figure 6a) showed a broad absorption band from  $3000$  to  $3500\text{ cm}^{-1}$ , confirming the presence of adsorbed hydroxyl species, free amino groups, and the nanosheet-based  $g\text{-C}_3\text{N}_4$  [37]. NCQDs also showed the same broad absorption band from  $2700$  to  $3800\text{ cm}^{-1}$ . Figure 6b shows the enlarged FTIR spectra for NCQD, CNS, and CNQD photocatalysts. The presence of aromatic C–N and C=N heterocycles on CNS and CNQD photocatalysts was confirmed by the solid absorption bands from  $1200$  to  $1800\text{ cm}^{-1}$ , located at  $1203$ ,  $1229$ ,  $1313$ ,  $1394$ ,  $1455$ ,  $1553$ , and  $1629\text{ cm}^{-1}$ , assigned to their skeletal stretching modes [65]. The absorption bands also confirmed the presence of C–N and C=N heterocycles on NCQDs at  $1192$ ,  $1388$ ,  $1551$ , and  $1656\text{ cm}^{-1}$ . The abovementioned

absorption bands also indicate the presence of various oxygen-containing functional groups: C–O ( $1000\text{--}1400\text{ cm}^{-1}$ ), C–O–C ( $1200\text{ cm}^{-1}$ ), and –COOH ( $1358\text{ cm}^{-1}$ ) [65,66]. The breathing mode of the triazine ring in CNS and CNQD photocatalysts was clearly observed at  $811$  and  $891\text{ cm}^{-1}$ . There were two functional groups observed in the NCQD: oxygenated functional groups and non-oxygenated groups, at positions  $1388\text{ cm}^{-1}$  (–COOH) and  $1551\text{ cm}^{-1}$  (C=O) [52]. These hydrophilic properties prove the stability and dispersibility properties of the NCQDs, which may have boosted the electron transport properties [49]. Furthermore, vibrations of non-oxygenated groups were located at  $1192\text{ cm}^{-1}$  (–C–NH–C) and  $1656\text{ cm}^{-1}$  (C=N) [49]. There were no additional bands in CNQD photocatalysts, which indicated that no impurities were present, similar to observations in previous studies [47,52]. There were no significant differences between CNS and CNQD photocatalysts, indicating that the chemical framework of CNQD composites was not altered when NCQDs were introduced on the surface of CNS [52].

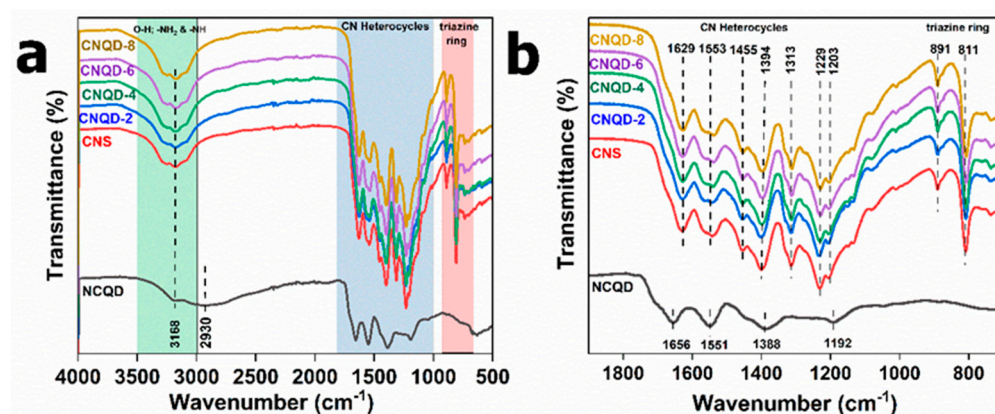


Figure 6. Full (a) and enlarged FTIR spectra (b) of NCQD, CNS, and CNQD photocatalysts.

The porous structure and specific surface areas of the prepared samples were analyzed using  $\text{N}_2$  adsorption–desorption at  $77\text{ K}$ . The adsorption–desorption isotherm results of CN and CNQD-6 are shown in Figure 7. CNS and CNQD samples exhibited a typical IV isotherm with a high adsorption capacity in the high relative pressure range of  $0.7\text{--}1.9\text{ P/P}_0$ , indicating the presence of abundant mesopores and macropores [67,68].

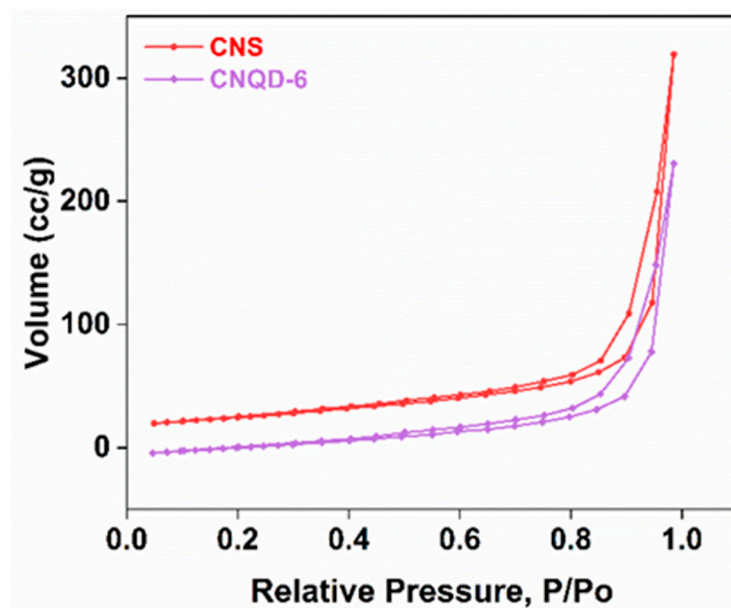


Figure 7.  $\text{N}_2$  adsorption–desorption isotherms of CNS and CNQD-6 photocatalysts.

The BET surface area, pore size, and pore volume of bCN, CNS, and CNQD photocatalysts are shown in Table 2. The specific surface area of CNS was  $81 \text{ m}^2/\text{g}$ , slightly higher than that of bCN, which was  $61 \text{ m}^2/\text{g}$ . The increased specific surface area of CNS, which probably provided more active sites for the adsorption of reactants, occurred due to the dissociation of bCN into a layer of sheet-like structure [69]. The change in the morphology of bCN compared with CNS can be considered a disadvantage of bCN, which is well known for its low surface area, large particle size, and fast charge carrier lifetime [70]. An increase in the surface area indicates a reduction in crystallite size and provides more active sites for the catalyst [71]. The pore size distribution peak of CNS was located at 9 nm, which is smaller than the bCN, located at 16 nm. The total pore volumes of bCN and CNS obtained were  $0.6 \text{ cm}^3/\text{g}$  and  $0.5 \text{ cm}^3/\text{g}$ , respectively. These results are similar to those observed in a previous study [68], which indicated that a two-step polymerization process can facilitate the formation of small pores during the entire polymerization process. The smaller pore size of CNS might be due to the well-formed and tight contact between the layer of CNS nanosheets, while the larger pore size might be due to the aggregation of the sphere bulk structure of bCN. The surface area of CNQD photocatalysts decreased with the increase in the weight percentage of NCQDs. This reduction is probably due to the hindered crystal growth of CNS consequent to the introduction of NCQDs. The significant changes in specific surface area after the addition of NCQDs also proved the regulation effects on the microstructure of CNQD photocatalyst. Small pores are favorable for the absorption of molecules, enhancing photocatalytic activity. The pore size for all CNQD photocatalysts was 2 nm, smaller than those of the pristine CNS, at 9 nm. This allows us to assume that the smaller porous structure of CNQD compared with CNS provides more active sites and slightly enhances the performance of photocatalytic degradation of DCF.

**Table 2.** Surface properties of bCN, CNS, and CNQD photocatalysts.

Sample	Surface Area ( $\text{m}^2/\text{g}$ )	Pore Size (nm)	Pore Volume ( $\text{cm}^3/\text{g}$ )
bCN	61	16	0.6
CNS	81	9	0.5
CNQD-2	78	2	0.5
CNQD-4	75	2	0.5
CNQD-6	69	2	0.4
CNQD-8	57	2	0.3

The XPS survey spectra in Figure 8a show that the main components of CNS and CNQD-6 were C, N, and O, with the binding energy peaks at 287.84, 398.84, and 531.84 eV, respectively. This is consistent with EA analysis results indicating that the main components of CNS and CNQD-6 were C and N. Other studies also revealed similar results [47,64]. Figure 8b shows the C 1s spectral peaks of CNS and CNQD-6, which highlight five peak points: (1)  $\text{sp}^2$  C–C bond at 284.8 eV; (2) C $\equiv$ N bond at 286.15 eV; (3)  $\text{sp}^2$ -bonded C atoms (N–C=N) at 288.3 eV; (4) N=C–O bond at 289.25 eV; and (5)  $\pi$ – $\pi$  bond at 293.74 eV [72]. There was no additional peak in the CNQD-6 photocatalyst spectrum, which provides further evidence for the successful incorporation of NCQDs into the CNS nanosheets. In addition, it is important to note that the peak positions of CNS did not shift after the introduction of NCQDs, as shown in CNQD-6, indicating that NCQDs did not connect to CNS via C-containing chemical bonds. Figure 8c shows the N 1s spectrum of CNS, which revealed three peaks, situated at 398.67, 399.92, and 401.00 eV, corresponding to  $\text{sp}^2$  of tri-s-triazine rings (C–N=C), bridged nitrogen atom groups (N $\equiv$ C), and amino functional group (C–N–H) bonds, respectively [61,73]. The slight shifts in the peaks of N1s spectra of CNQD-6 situated at 398.30, 399.56, and 400.65 eV after the addition of NCQDs suggested that NCQDs might load onto the surface of CNS via the formation of C–N=C, N $\equiv$ C, and N–H bonds, while the original structure of CNS almost did not change, which is similar to the reported results in the literature [69].

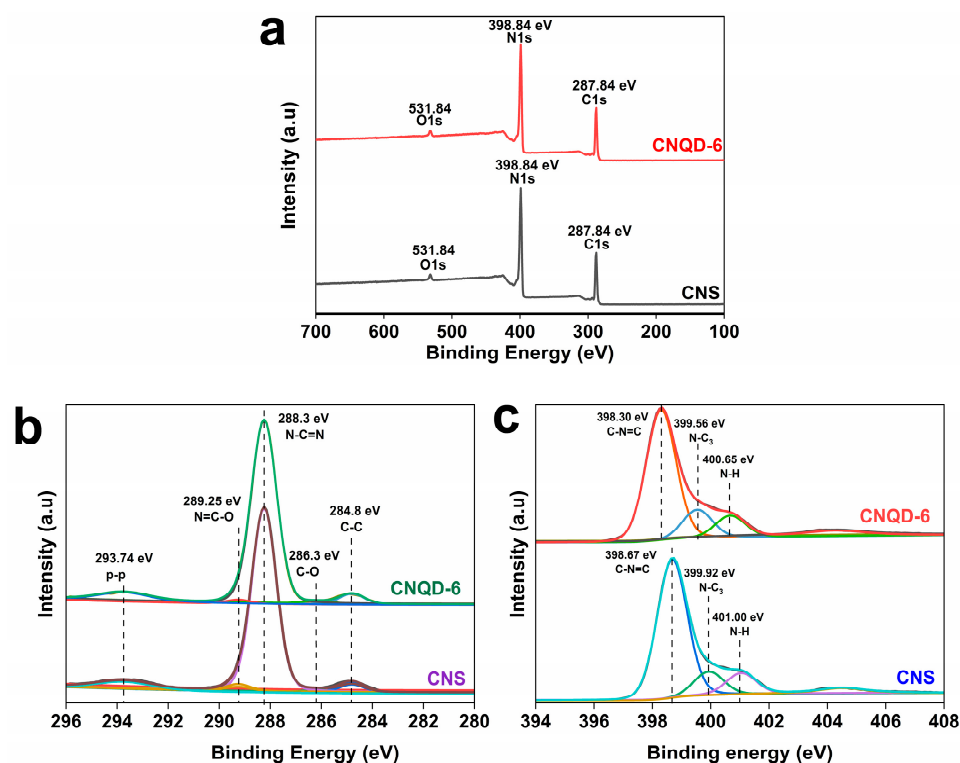


Figure 8. XPS spectra (a), C 1s spectral peak (b), and N 1s spectrum (c) of CNS and CNQD-6 photocatalysts.

## 2.2. Physicochemical and Photoelectrochemical Measurements

The UV/Vis diffuse reflectance spectra (UV/Vis-DRS) of NCQD, bCN, CNS, and CNQD photocatalysts are depicted in Figure 9. The absorption edges of bCN and CNS (Figure 9a) were around 461 nm and 445 nm, similar to other reported studies [52,58,74]. The absorption edges of CNQD composites (Figure 9a) were in the range of about 461 to 475 nm, indicating a slight increase compared with CNS, which is in agreement with a previous study [74]. Light absorption enhancement could be due to the synergistic effect and intrinsic charge generation between CNS and NCQDs, which helps generate more photogenerated electrons [65,75]. The Tauc Plot graph in Figure 9b shows that the band gap values of bCN and CNQD photocatalyst samples were between 2.65 eV and 2.76 eV, while the band gap of CNS was 2.80 eV. The wavelength of NCQDs was more than 1200 nm, while its band gap was less than 1.00 eV, similar to what has been reported in [52]. Therefore, the addition of NCQDs did not substantially affect the band gap of CNQD photocatalysts.

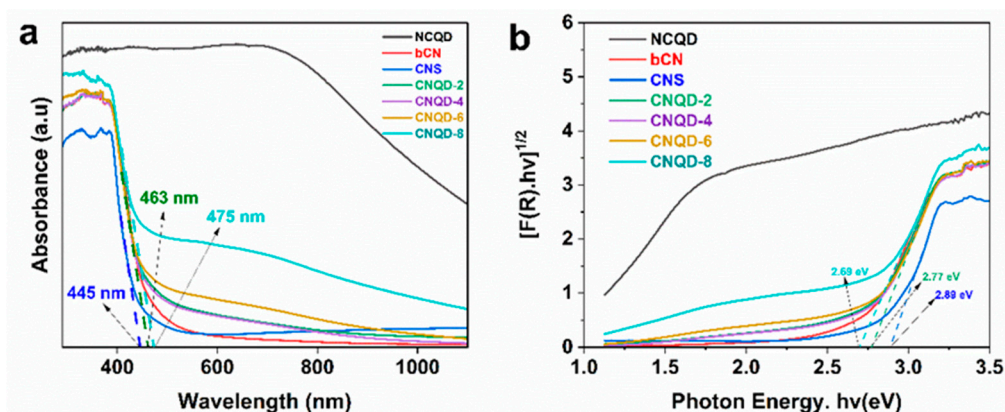


Figure 9. UV/Vis-DRS (a) and Tauc plots (b) of NCQD, bCN, CNS, and CNQD photocatalysts.

The photoluminescence (PL) spectra in Figure 10 show the results of the analysis of the radiative recombination rate of bCN, CNS, and CNQD photocatalysts. The purpose of PL spectrum measurements was to determine the nature of radiative recombination activity and charge kinetics of the synthesized photocatalysts. A photocatalyst is generally activated to generate holes and electrons when exposed to the excitation light during PL tests. As a result, as photoluminescence intensity decreased, electron and hole recombination decreased, and the ability of the sample to extract charges improved. As shown in Figure 10, bCN and CNS showed intense and broad PL emission peaks, indicating the rapid recombination of electron–hole pairs through band–band transitions. In addition, CNQD photocatalysts showed significantly reduced PL intensities relative to bCN and CNS. The reduction in PL intensity is due to the effective interfacial charge separation in CNQD photocatalysts from well-formed interfaces, suppressing the charge recombination. These results align with the findings of previous studies [76].

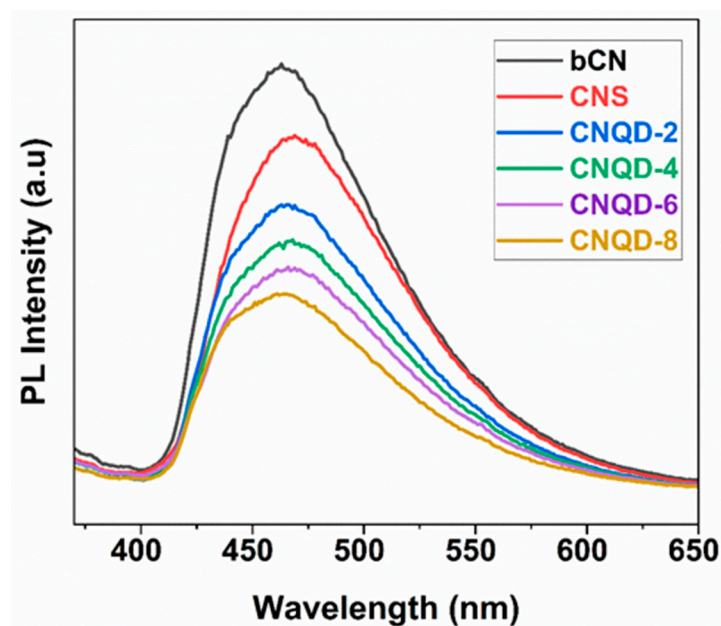
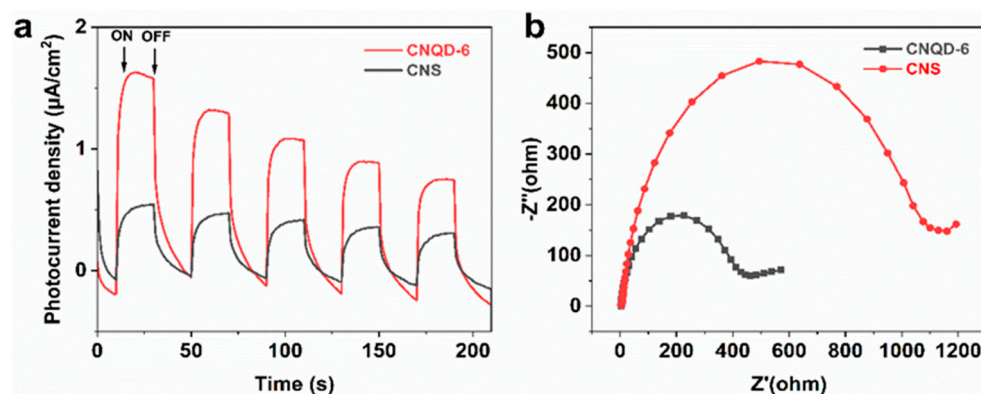


Figure 10. PL spectra of bCN, CNS, and CNQD photocatalysts.

The results of the transient photocurrent density (TPD) investigations of CNS and CNQD-6 photocatalysts are illustrated in Figure 11. The measured transient photocurrent was plotted with respect to time (Figure 11a) for CNS and CNQD-6, with alternate cycles of on–off visible light irradiation to study their photoelectronic properties. The electric current generated by the photoexcited charge carriers was measured using transient photocurrent. The visible light pulse was turned on and immediately decayed with the light shut off. The current density (Figure 11a) measured for CNQD-6 was relatively high compared with CNS, which could be attributed to strong electron separation efficiency [52]. The boosted effectiveness in electron–hole pair separation for CNQD-6 may be ascribed to the presence of NCQDs on the surface of CNS. In the CNQD-6 photocatalyst, electron migration occurred from NCQDs to CNS, effectively hindering the recombination of electron–hole pairs [77]. This result confirms the ability of NCQDs to act as electron reservoirs to capture photoexcited electrons and channels for electron transport, which leads to higher charge separation efficiencies [52,78]. This observation is in good agreement with the PL test results, which were discussed earlier and shown in Figure 10.



**Figure 11.** Transient photocurrent responses versus time (a) and EIS Nyquist plots (b) of CNS and CNQD-6 photocatalysts.

Electrochemical impedance spectroscopy (EIS) was also conducted to study the interfacial charge transfer properties of CNS and CNQD-6, as shown in Figure 11b. In Nyquist plots, the magnitude of the semi-circular curve indicates the extent of the charge transfer resistance of the electrode surface, where a larger arc radius indicates higher resistance [24,79]. The arc resistance ( $-Z''$ ) of CNQD-6 (Figure 11b) was relatively lower than that of CNS, indicating that it possessed better charge transfer capacity [52]. The lower resistance in CNQD-6 implies the contribution of NCQDs to the effective separation of electron-hole pairs [52,78].

### 2.3. Photocatalytic Activity Measurements

Figure 12 illustrates the photocatalytic activity of bCN, CNS, and CNQD photocatalysts based on the degradation of DCF. The adsorption–desorption equilibrium between DCF and the photocatalysts was reached in the dark after 30 min, but almost no adsorption was observed. The photocatalytic tests were conducted for three hours under visible light irradiation. The same procedures were used for the control experiments (catalyst-free), as shown in Figure 12a. DCF was not significantly photolyzed, further confirming the importance of photocatalysts in the photodegradation process. As shown in Figure 12a, only 50% of DCF could be removed using bCN, while CNS removed 53% after 180 min. This observation is in good agreement with the morphology, structure, and physicochemical results, which were discussed earlier. After 180 min of exposure, the CNQD photocatalyst demonstrated increased photocatalytic degradation efficiency (%), with 54, 54, 62, and 56 for CNQD-2, CNQD-4, CNQD-6, and CNQD-8, respectively. The efficiency enhancement (%) of CNQD composites compared with the pristine CNS is in good agreement with the photoelectrochemical results (Figure 11), which confirm the contribution of NCQDs to enhancing electron separation efficiency. An overview of the photodegradation efficiencies and kinetic rate constants of bCN, CNS, and CNQD-6 is shown in Figure 12b. The photocatalytic performance was found to be in the following order: CNQD-6 > CNS > bCN. The CNQD-6 photocatalyst significantly improved photoactivity, compared with bCN and CNS under visible light irradiation. As stated above, NCQDs on the surface of CNS could both enhance visible light absorption and improve the charge separation of  $h^+$  and  $e^-$ . However, an excessive number of NCQDs could lead to a shield effect and inhibit photocatalysis, as also indicated in previous reports [50]. As a result, the DCF photodegradation of CNQD-8 decreased even with higher NCQD loading. Therefore, the optimum composite was CNQD-6, which removed 62% of DCF in 180 min and had a  $k$  value of  $5.41 \times 10^{-3} \text{ min}^{-1}$  and an improvement factor of 1.24 over bCN. CNQD-6 had the highest photocatalytic activity and thus was used for subsequent tests.

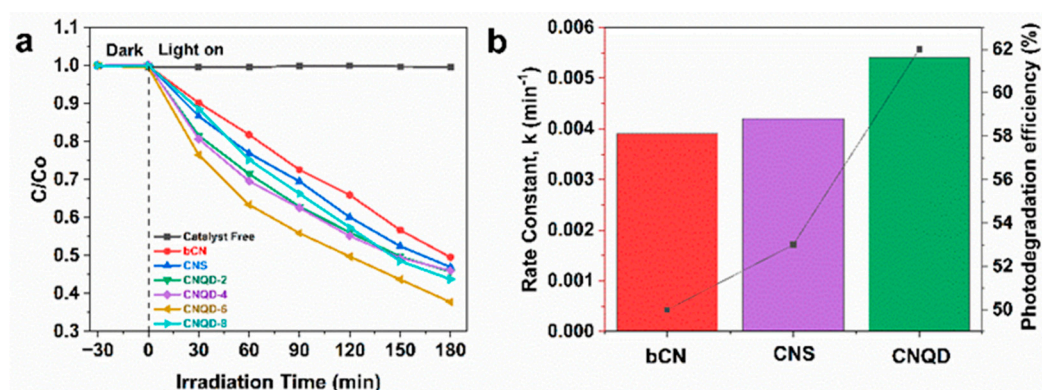


**Figure 12.** Photolysis of DCF (a) using bCN, CNS, and CNQD photocatalysts; DCF degradation efficiency and kinetic rate constant of each photocatalyst under the irradiation of visible light (b).

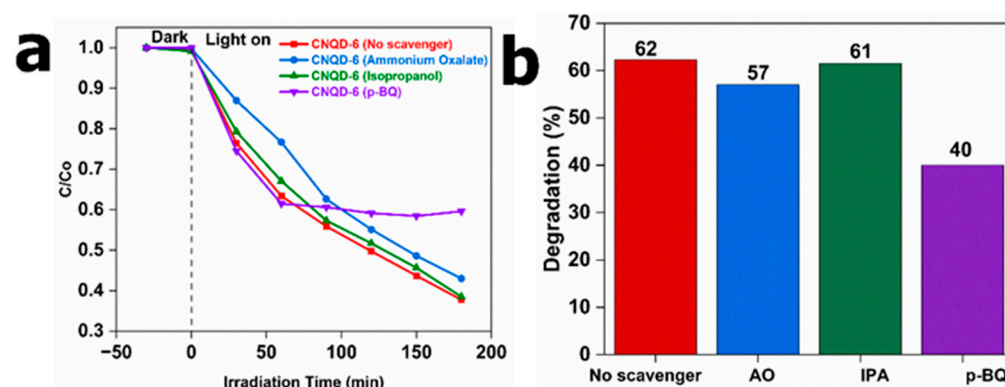
Table 3 shows a comparison of several g-C<sub>3</sub>N<sub>4</sub>-based photocatalysts, with their initial DCF concentrations and first-order kinetics of DCF degradation. In 2018, Jianyang Sun et al. reported that the g-C<sub>3</sub>N<sub>4</sub>/BiVO<sub>4</sub> catalyst degraded DCF via a photoelectrochemical reaction with a first-order kinetic rate ( $k$ ) of  $3.20 \times 10^{-3} \text{ min}^{-1}$  [29]. The initial pH and DCF concentrations were 3.17 and  $10 \text{ mg L}^{-1}$ , respectively. In that report, it was mentioned that a lower pH value and a lower initial DCF concentration led to better degradation efficiency. Furthermore, the report suggested that, at low pH levels, H<sup>+</sup> ions react with OH<sup>-</sup> and promote the reaction of •OH, thus facilitating the degradation of DCF. In 2019, Wen Liu et al. reported that the CQD-modified porous g-C<sub>3</sub>N<sub>4</sub> catalyst removed DCF via a photocatalytic reaction with a first-order kinetic rate ( $k$ ) of  $7.4 \times 10^{-2} \text{ min}^{-1}$  [50]. In contrast, that report indicated that higher pH values facilitate the degradation of DCF under visible light irradiation. Under alkaline conditions, the enhanced adsorption of OH<sup>-</sup> affects the electronegativity of atoms on the surface of the catalyst and contributes to the generation of •O<sub>2</sub><sup>-</sup>. In another study, Wei Zhang et al. reported a first-order kinetic rate ( $k$ ) of  $4.53 \times 10^{-1} \text{ min}^{-1}$  for the photocatalytic degradation of DCF using a Ag<sub>3</sub>PO<sub>4</sub>/g-C<sub>3</sub>N<sub>4</sub> catalyst [44]. In that report, the initial concentration of DCF was  $1 \text{ mg L}^{-1}$ , and the pH was not adjusted. In 2020, Tahereh et al. reported that porous carbon nitride (mp-CN) was removed from DCF via photocatalytic degradation with a first-order kinetic rate ( $k$ ) of  $4.90 \times 10^{-3} \text{ min}^{-1}$  at a  $40 \text{ mg L}^{-1}$  initial DCF concentration [25]. Based on that report, DCF degradation decreased with an increase in the initial concentration of DCF. The high concentration of DCF might excessively be adsorbed on the photocatalyst layer, hindering light adsorption and the oxidation process. The higher effectiveness in DCF degradation at  $10 \text{ mg L}^{-1}$  may result from a higher oxidation level reached by the generated by-products, as reported by [80,81]. In the latest report in 2022, Ying Yan et al. reported that ruthenium-doped g-C<sub>3</sub>N<sub>4</sub> (CNRu) is an efficient catalyst for peroxymonosulfate (PMS) activation in DCF photocatalytic degradation [45]. The initial pH value and DCF concentration were 3.80 and  $10 \text{ mg L}^{-1}$ , respectively. This report mentioned that the pH had a negligible effect on DCF removal in a wide range of pH, from 3.00 to 9.00. The slight negligible enhancement in DCF degradation is mainly due to the electrostatic adsorption of a catalyst under acidic conditions. The effects of pH will only become more complex if a heterogenous catalyst is used because pH can affect the physicochemical properties of catalysts, which is in line with previous reports [82,83]. In this case, without adjusting the initial pH and considering the low concentration of DCF, CNQD-6 in our study revealed superior performance under visible light irradiation, as indicated in the results of g-C<sub>3</sub>N<sub>4</sub>-based composites in Table 3.

**Table 3.** Comparison of degradation performance of DCF with the cited studies.

g-C <sub>3</sub> N <sub>4</sub> -Based Composite	Initial DCF Concentration	First Order Kinetics, $k$ (min <sup>-1</sup> )	Reference
CNQD	$C_0 = 20 \text{ mg L}^{-1}$	$5.41 \times 10^{-3}$	This work
g-C <sub>3</sub> N <sub>4</sub> /BiVO <sub>4</sub>	$C_0 = 10 \text{ mg L}^{-1}$	$3.20 \times 10^{-3}$	[29]
CQD-modified porous g-C <sub>3</sub> N <sub>4</sub>	$C_0 = 10 \text{ mg L}^{-1}$	$7.40 \times 10^{-2}$	[50]
Ag <sub>3</sub> PO <sub>4</sub> /g-C <sub>3</sub> N <sub>4</sub>	$C_0 = 1 \text{ mg L}^{-1}$	$4.53 \times 10^{-1}$	[44]
mp-CN	$C_0 = 40 \text{ mg L}^{-1}$	$4.90 \times 10^{-3}$	[25]
CNRu	$C_0 = 10 \text{ mg L}^{-1}$	$3.20 \times 10^{-2}$	[45]

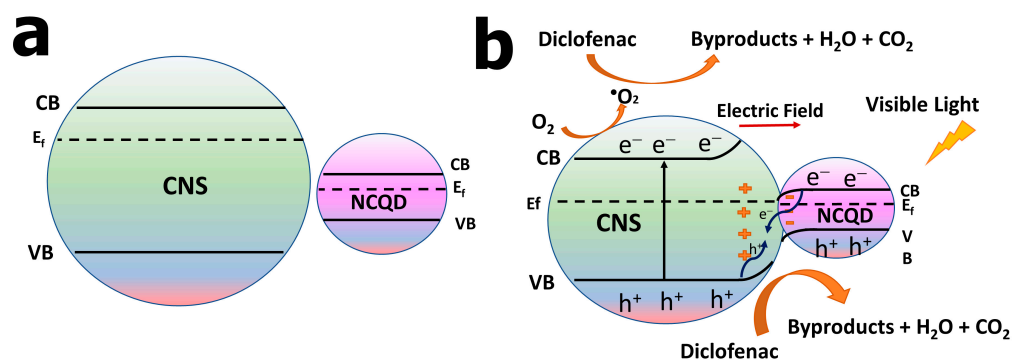
#### 2.4. Reactive Species Detection and Identification of Degradation Intermediates

Figure 13 illustrates the influence of scavengers on the kinetics of DCF degradation via scavenger experiments. With scavenging studies, it was possible to determine the contribution of each reactive species to the photodegradation of DCF and suggest a possible photocatalytic mechanism for the photocatalysts. The declined photocatalytic performance in the presence of each scavenger highlights the importance of the associated reactive species. The essential reactive species of  $h^+$ ,  $\bullet\text{OH}$ , and  $\bullet\text{O}_2^-$  were assumed to be captured by the scavenging compounds AO, IPA, and *p*-BQ. As shown in Figure 13a, adding *p*-BQ (a scavenger of  $\bullet\text{O}_2^-$ ) caused a drop in photodegradation performance (%), indicating that  $\bullet\text{O}_2^-$  species were required for DCF photodegradation. In addition, it was found that the addition of AO (an  $h^+$  scavenger) had almost little effect on the kinetics of this photodegradation reaction. Therefore, it was concluded that the superoxide radical ( $\bullet\text{O}_2^-$ ) in CNQD-6 significantly influenced its photodegradation kinetics. This outcome is consistent with the results reported in [50].



**Figure 13.** Photolysis of DCF with different scavengers (AO, IPA, and *p*-BQ) on degradation kinetics (a), and influence of scavengers on photocatalytic efficiency over bCN, CNS, and CNQD photocatalysts under visible light irradiation (b).

According to the results of UV/Vis measurement (Figure 9), the band gaps of CNS and NCQDs were 2.89 and 1.00 eV, respectively. Based on UV/Vis and scavenging test data, a plausible step-by-step charge transfer mechanism for DCF photodegradation is shown in Scheme 1. Scheme 1a shows the Fermi level ( $E_f$ ) of NCQDs and CNS, respectively, when they were not in contact. The  $E_f$  of NCQDs was lower (more positive) than that of CNS. In contrast, Scheme 1b shows the aligned structure of  $E_f$  NCQDs and  $E_f$  CNS when they were in direct contact. The aligned  $E_f$  occurred due to the free electron transfer from CNS with a high  $E_f$  through the interface to NCQDs with a low  $E_f$  until they achieved the same level. The  $E_f$  alignment generated an interfacial electric field (E.F), with a direction from CNS to NCQDs, and band bending (Scheme 1b). The energy band edge of NCQDs (low  $E_f$ ) was bent downward, whereas that of CNS (high  $E_f$ ) was continuously bent upward toward the interface [84]. The E.F and band bending acted as barriers to prevent the electrons from transferring from CNS to NCQDs and the holes from transferring from NCQDs to CNS.



**Scheme 1.** Schematic illustration of band positions of separated CNS and NCQD (a), and narrow sense photocatalytic degradation of DCF when CNS and NCQD are in contact (CNQD) (b).

Under visible light irradiation, the electrons of NCQDs and CNS were activated. The photogenerated electrons in the CB of NCQDs flew out and combined with the holes in the valence band (VB) of CNS, thus maintaining those holes with a high oxidation potential and enhancing the separation of charge carriers. The higher separation of the charge carriers of CNQD-6, compared with pristine CNS, is reflected in the PL and TPD results in Figures 10 and 11, respectively. This resulted in the accumulation of photogenerated electrons in CB of CNS and photogenerated holes in VB of NCQDs and CNS. The photogenerated electrons in CB of CNS reacted with O<sub>2</sub>-producing superoxide radicals ( $\bullet\text{O}_2^-$ ), which decomposed the DCF. In addition to the direct reaction with DCF, a small portion of  $\bullet\text{O}_2^-$  would transfer into  $\bullet\text{OH}$ , thus slightly contributing to DCF decomposition. The holes in CNQD composites also played a role in the decomposition of DCF. These findings are in good agreement with the results of scavenger experiments in Figure 13.

A combination of NCQDs and PrFeO<sub>3</sub> for Z-scheme photocatalysis was reported in [57]. In that report, Xiazhang Li et al. revealed that NCQDs (with low E<sub>f</sub>) moderated the transfer of interfacial charges and generated band bending when connected with a high-E<sub>f</sub> semiconductor, highlighting the significance of the generated Z-scheme photocatalysis. NCQDs can also be considered photosensitizers under visible light irradiation, as reported in [50]. In that report, Wen Liu et al. suggested that CQDs work as a transfer bridge between the photoexcited electrons on DCF molecules and g-C<sub>3</sub>N<sub>4</sub> on the surface under visible light irradiation. The accumulated activated electrons on the CB of g-C<sub>3</sub>N<sub>4</sub> then react with O<sub>2</sub>-producing superoxide radicals ( $\bullet\text{O}_2^-$ ) and decompose the DCF. In this context, the charge migration pathway of CNQDs under visible light irradiation remained the same in our study (from NCQDs to CNS).

Figure 14 shows the results of the TOC removal of DCF and the reusability test of the CNQD-6 photocatalyst. Figure 14a shows the TOC removal (%) of DCF over the CNQD-6 in 3 h, 5 h, and 6 h reaction times. The TOC removal of the reaction suspension was found to be increased from 34 to 55 and 75 during 5 h and 10 h reactions, respectively. This indicates that an increase in reaction time enhances DCF mineralization. Figure 14b shows the removal of DCF by CNQD-6 in three consecutive cycles, which was measured using HPLC. The second and third cycles reduced DCF to 55% and 51%, respectively. This shows that the removal efficiency of CNQD-6 was reduced by about 10% even in the third cycle. This result reveals its excellent reusability and photostability properties, similar to the reported literature [50,85]. The C–N=C sp<sub>2</sub>-hybridized aromatic N atoms were reported as critical components of g-C<sub>3</sub>N<sub>4</sub>, which is associated with the in-plane  $\pi$ -conjugated bond and plays a significant role in absorption, a closely related mechanism to photocatalytic performance [86]. Only a slight loss was observed in the C–N=C bond during the photostability test, as reported in [85], indicating the excellent stability properties of g-C<sub>3</sub>N<sub>4</sub>.

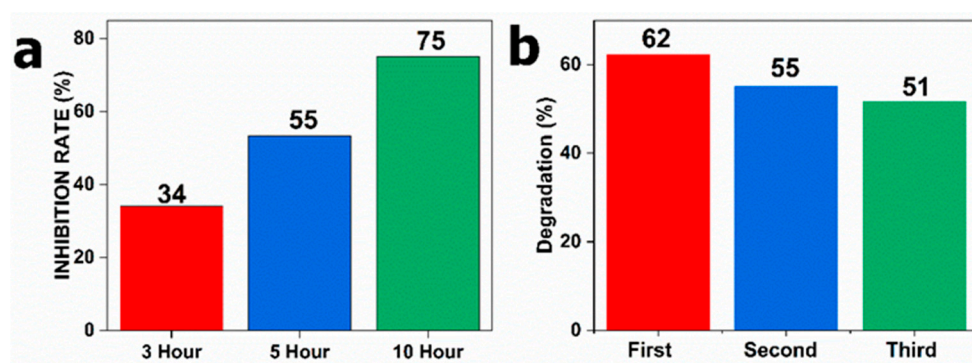


**Figure 14.** TOC removal during photocatalysis of DCF over CNQD-6 (a), and removal of DCF by CNQD-6 in three consecutive cycles (b).

### 3. Materials and Methods

#### 3.1. Chemicals and Instruments

Urea ( $\geq 99.5\%$ ), citric acid ( $\geq 99.5\%$ ), diclofenac sodium (DCF,  $\geq 99\%$ ), ammonium oxalate monohydrate ( $(\text{NH}_4)_2\text{C}_2\text{O}_4 \cdot \text{H}_2\text{O}$ ,  $\geq 99\%$ ), *p*-benzoquinone ( $\text{C}_6\text{H}_4\text{O}_2$ ,  $>98\%$ ), and isopropanol ( $\text{C}_3\text{H}_8\text{O}$ ,  $99.9\%$ ) were used without further purification as received from commercial sources (Sigma-Aldrich, St. Louis, MO, USA, and Merck, Darmstadt, Germany). The instruments used to prepare the photocatalysts were an ultrasonic bath (S 60 H, Elma Schmidbauer GmbH, Singen, Germany), a furnace (Nabertherm, Lilienthal, Germany), a freeze-dry oven (Christ Alpha 2-4 LSCbasic, Martin Christ Gefriertrocknungsanlagen GmbH, Osterode am Harz, Germany), and a PTFE-lined autoclave (DAB-2, Berghof Products + Instruments GmbH, Eningen, Germany).

#### 3.2. Preparation of Bulk $g\text{-C}_3\text{N}_4$ and $g\text{-C}_3\text{N}_4$ Nanosheets

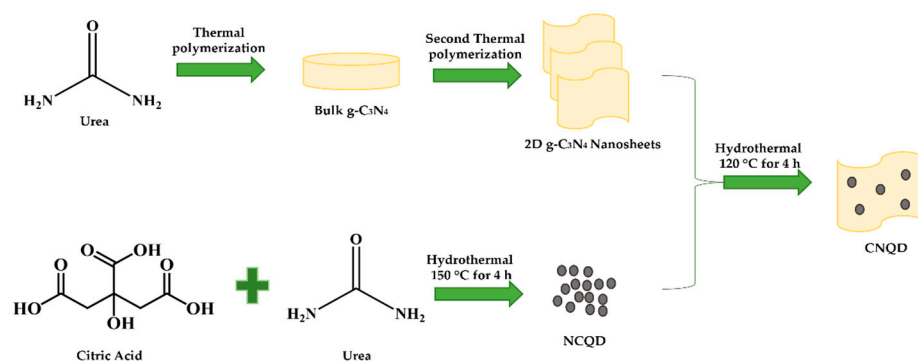
The synthesis of the bulk  $g\text{-C}_3\text{N}_4$  via the thermal polymerization of urea was conducted based on a previously reported method [65]. Briefly, 10 g of urea was put in a 50 mL porcelain crucible, completely covered with a lid, and heated to  $550\text{ }^\circ\text{C}$  at a ramping rate of  $300\text{ K/h}$ . This temperature was then sustained for 3 h at  $550\text{ }^\circ\text{C}$ . After cooling to room temperature, 0.65 g of a bright-yellow solid was obtained. This was crushed into powder and labeled as the bulk  $g\text{-C}_3\text{N}_4$  (bCN) sample. Afterward, the synthesized bCN was subjected to a second process of heat polymerization with a partially covered porcelain crucible. The initial conditions for thermal polymerization, such as the ramping rate, final temperature, and duration, were held constant. The resulting 0.53 g light-yellow substance was again crushed to powder and marked as the  $g\text{-C}_3\text{N}_4$  nanosheet (CNS) sample. Table 1 shows the elemental analysis results of bCN and CNS. bCN contained C 29.4, H 2.0, and N 55.9 (wt%), while CNS contained C 31.1, H 3.8, and N 59.3 (wt%).

#### 3.3. Preparation of Nitrogen-Doped Carbon Quantum Dots (NCQDs)

The synthesis of NCQDs was performed via the hydrothermal treatment of urea and citric acid, as previously reported in the literature [52], with minor modifications. In 15 mL of deionized water, 3 g of citric acid and 1 g of urea were combined and dissolved. After being stirred at 500 rpm for 30 min at room temperature, the mixture was heated at  $150\text{ }^\circ\text{C}$  for 4 h in a PTFE-lined autoclave. The resulting dark-brown solution was centrifuged at 12,000 rpm for 20 min. Afterward, the solution was filtered using an ultrafiltration membrane ( $M_w\text{CO} = 2000$ ) to remove impurities. The final dark solution was subjected to freeze-drying to obtain the solid NCQD samples. Thus, 0.55 g of NCQD powder was obtained, and the result from elemental analysis in wt% shows that it contained C 36.0, H 6.3, and N 14.7, as shown in Table 1.

### 3.4. Preparation of CNQD Photocatalysts

The synthesis of CNQD catalysts with different NCQD concentrations (2, 4, 6, and 8 wt%) was carried out using the hydrothermal method (120 °C, 4 h). In detail, 1 g of CNS was ultrasonically treated in 90 mL of deionized water for 30 min at room temperature to exfoliate and delaminate its sheet's structure. Next, ultrasonication was performed for 15 min to disperse NCQDs in 10 mL of distilled water. After that, these two solutions were mixed and stirred at room temperature for 30 min. Then, the mixture was put into a PTFE-lined autoclave reactor and heated to 120 °C for 4 h. The precipitate was collected, washed three times with distilled water, centrifuged at 6000 rpm for six minutes, and dried at 70 °C in a drying oven overnight. The prepared CNQD composites were denoted as CNQD-2, CNQD-4, CNQD-6, and CNQD-8, which indicate the different NCQD concentrations (2, 4, 6, and 8 wt%); these composites were then incorporated into the CNS sample. The hydrothermal route to synthesize CNQDs is depicted in Scheme 2.



**Scheme 2.** Schematic illustration of the synthesis of CNQD photocatalysts.

As depicted in Scheme 2, the synthesis was completed in three simple steps. First, urea was chosen as a precursor to prepare bCN via thermal polymerization. The bCN sample then underwent a second round of thermal polymerization to modify its morphology into 2D  $g\text{-C}_3\text{N}_4$  nanosheets, denoted as CNS. NCQDs were synthesized using citric acid and urea in the second step. The collected NCQD powder was then added to the surface of CNS as a co-catalyst via the hydrothermal method (120 °C, 4 h), which was denoted as the CNQD photocatalyst. The physicochemical and photoelectrochemical properties of CNQD photocatalysts improved compared with bCN, as shown in the results of complementary characterization analysis.

### 3.5. Characterization

The structural and morphological features of the catalysts were assessed via scanning electron microscopy (SEM) and energy-dispersive X-ray (EDX) analysis. The SEM micrographs were recorded using a Merlin VP compact device (Zeiss, Oberkochen, Germany), and the EDX analysis was carried out using Bruker Quantax (Bruker Corporation, Billerica, MA, USA).

The X-ray diffraction (XRD) powder patterns were recorded on an Xpert Pro diffractometer (Panalytical, Almelo, The Netherlands) equipped with an Xcelerator detector using automatic divergence slits and  $\text{CuK}\alpha_1\text{K}\alpha_2$  radiation (40 kV, 40 mA;  $\lambda_1 = 0.15406$  nm;  $\lambda_2 = 0.15443$  nm). The obtained intensities were converted from automatic to fixed divergence slits ( $0.25^\circ$ ) for further analysis. Phase identification was carried out using the database of the International Center of Diffraction Data (ICDD, Newtown Square, PA, USA).

The X-ray photoelectron spectroscopy (XPS) was conducted using a photoelectron spectrometer (Multilab 2000, Thermo Fisher Scientific, Waltham, MA, USA) with  $\text{Al K}\alpha$  radiation as the excitation source. All XP spectra refer to the  $\text{C}1s$  line at 284.6 eV.

Elemental analysis (C, H, and N) was performed using atomic absorption spectroscopy (AAS) with PerkinElmer AAS-Analyst 300 spectrometers (Waltham, MA, USA) at the

elemental analysis laboratory, LIKAT Rostock. The samples were prepared for analysis using acid digestion with  $\text{H}_2\text{SO}_4/\text{KHSO}_4$ .

Fourier transform infrared spectroscopy (FTIR, Nicolet 330, Thermo Fisher Scientific, Waltham, MA, USA) was performed under ambient conditions using KBr as a background.

UV/Vis spectroscopy in diffuse reflectance (DRS) was measured using a Lambda 365 UV/Vis spectrophotometer (PerkinElmer, Waltham, MA, USA) with an integrating sphere to study the light absorption properties of all the samples in a range of 190 to 1100 nm.

The photoluminescence (PL) of the catalysts was analyzed using a fluorescence spectrophotometer (Agilent Technologies Inc., Mulgrave, Australia) at room temperature with an excitation wavelength of 350 nm, and the range was 370 to 680 nm.

The specific surface areas of all the samples were determined via nitrogen physisorption according to the Brunauer–Emmett–Teller (BET) method using a BELSORP max II (Microtrac Retsch GmbH, Haan, Germany) and a NOVAtouch (Anton Paar Germany GmbH, Ostfildern-Scharnhausen, Germany). Before the measurement, the samples were degassed at 200 °C for 5 h.

### 3.6. Photoelectrochemical Analyses

The photoelectrochemical experiments were performed using the Zennium electrochemical workstation equipped with a PP211 CIMPS system (Zahner, Kronach, Germany) with typical three-electrode cells. The 0.5 M sodium sulfate solution of pH 7.0 served as the electrolyte in this measurement. The reference electrodes were saturated Ag/AgCl (3M, NaCl), while the counter-electrodes were platinum wires. To create a thin coating layer and a functional electrode, 20 mg of the photocatalyst was dispersed in a mixture of 100  $\mu\text{L}$  Nafion solution (5 wt.%) and 900  $\mu\text{L}$  isopropyl alcohol, and then the dispersion was drop-cast on an active area of  $1.5 \times 1.5 \text{ cm}^2$  ITO glass after being dispersed in ethanol for 10 min using ultrasonication. A 430 nm LED lamp ( $400 \text{ mW}/\text{cm}^2$ ) was used as a light source for all photoelectrochemical tests. The photocurrent response curves were generated with the light on and off every 20 s. Electrochemical impedance spectroscopy (EIS) was carried out using a potential static method in the frequency range of 0.01 to 100 kHz.

### 3.7. Photodegradation Experiments

The photodegradation of diclofenac under visible light irradiation was carried out in a double-jacketed-glass cylindrical batch photoreactor ( $V = 120 \text{ mL}$ , Hassa Labor, Lübeck, Germany). The Xe arc lamp (300 W) was equipped with a reflector system (LOT Quantum Design, Darmstadt, Germany) and a 420 nm filter to irradiate the suspension. The 6 cm distance between the reflector system and the reactor was fixed to irradiate the reaction mixture from the top. The photocatalytic experiments were conducted at a constant temperature (25 °C) and stirring speed (500 rpm). For each experiment, 50 mg of catalyst was dispersed in 50 mL of a DCF aqueous solution ( $C_0 = 20 \text{ mg L}^{-1}$ ), followed by stirring (500 rpm) for 30 min under airflow before irradiation to ensure that the catalyst and DCF had established an equilibrium for adsorption and desorption. At set intervals during the photodegradation process, the samples were taken and filtered for further evaluation (0, 30, 60, 90, 120, 150, and 180 min). DCF transformation was analyzed using high-performance liquid chromatography (HPLC, Agilent Technologies, 1260 Infinity Series, Santa Clara, CA, USA). The mineralization efficiency was assessed after a 3 h reaction by evaluating the total organic carbon content (TOC) of the filtered (0.22 mm) reaction mixture. The dissolved carbonate content from the CNQD catalyst was quantified with the organic carbon content of the reaction mixture (IC) using a TOC analyzer (multi N/C, 3100, Analytik Jena, Jena, Germany). Following the Langmuir–Hinshelwood model, the photocatalytic pseudo-first-order reaction rate constant ( $k$ ) was calculated using Equation (1), where  $C_0$  ( $\text{mg L}^{-1}$ ),  $C$  ( $\text{mg L}^{-1}$ ),  $k$  ( $\text{min}^{-1}$ ), and  $t$  (min) define the initial DCF concentration, the DCF concentration

at time  $t$ , the kinetic rate constant, and the irradiation time, respectively. The effectiveness of the photocatalysts was assessed using Equation (2).

$$\ln \frac{C_0}{C} = kt \quad (1)$$

$$\frac{C_0 - C}{C_0} \times 100\% \quad (2)$$

The photocatalytic stability of the optimum NCQD was assessed by carrying out three rounds of DCF photodegradation tests. First, the photocatalysts were collected via centrifugation, filtered through a 0.22  $\mu\text{m}$  membrane, and then dried for 12 h at 60 °C after each round.

The same experimental conditions were applied during the scavenging experiments to investigate the possible photocatalytic processes using isopropanol (IPA), ammonium oxalate (AO), and *p*-benzoquinone (*p*-BQ). IPA, AO, and *p*-BQ were separately added to the reaction system to quench hydroxyl radicals ( $\bullet\text{OH}$ ), photogenerated holes ( $h^+$ ), and superoxide radicals ( $\bullet\text{O}_2^-$ ), respectively. In this step, 50 mg of catalyst was dispersed in 25 mL of the DCF aqueous solution ( $C_0 = 40 \text{ mg L}^{-1}$ ). Then, another 25 mL volumes of IPA, AO, and *p*-BQ were separately added. The scavenger activity influenced the photocatalytic activity, as reflected in the mechanism of the related reactive species.

#### 4. Conclusions

In summary, NCQDs were successfully incorporated into the surface of CNS nanosheets for the photocatalytic degradation of DCF under visible light irradiation. The successful modification of pristine CNS was verified with characterization studies such as EA, FESEM, EDX, XRD, FTIR, the adsorption–desorption isotherm test, and XPS to observe the changes in its morphology and structure. The UV/Vis-DRS analysis also showed an improvement in the CNQD composites' optical properties, according to which the CNQD composites exhibited higher absorption intensity than pristine bCN and CNS. The test results of the photocatalytic degradation of DCF revealed that the 6 wt% NCQD (CNQD-6) had the optimal performance, which removed 62% of DCF in 3 h and had a first-order kinetic rate constant  $k = 5.41 \times 10^{-3} \text{ min}^{-1}$  under visible light irradiation. These results confirmed the contribution of NCQDs to enhancing photocatalytic activity, leading to an improvement factor of 1.24 over bCN. We believe the enhanced photocatalytic properties of the optimum CNQD-6 occurred due to the synergistic effects of increased charge density to facilitate rapid charge migration, reduced electron–hole recombination rates, and an optimized interface between NCQDs and CNS. Photoelectrochemical measurements, including the TPR and EIS Nyquist plots, elucidated these phenomena. NCQDs increased the optical properties of the pristine CNS by promoting effective charge transfer and increasing the charge mobility to promote the separation of electron–hole pairs. Through scavenger experiments, we found that the photogenerated superoxide ( $\bullet\text{O}_2^-$ ) radicals predominated in the degradation of DCF. In addition, toxicity reduction and reusability tests demonstrated that the NCQD composites exhibited good photostability properties. This work provides insight into the effects of NCQDs on the surface of CNS; notably, they enhance the potential of CNS to remove emerging organic pollutants from water and wastewater.

**Author Contributions:** Conceptualization, H.A., T.P. and J.S.; methodology, H.A. and T.P.; formal analysis, H.A.; investigation, H.A.; writing—original draft preparation, H.A.; writing—review and editing, H.A., T.P. and J.S.; supervision, T.P. and J.S. All authors have read and agreed to the published version of the manuscript.

**Funding:** This research received no external funding.

**Data Availability Statement:** Data are contained within the article.

**Acknowledgments:** Huzaikha Awang gratefully acknowledges the scholarship Graduate Excellence Program (GrEP) provided by Majlis Amanah Raya, MARA Malaysia. The Analytical Department of LIKAT is gratefully acknowledged. In addition, the authors thank Shuoping Ding (LIKAT), Felix Lorenz (LIKAT), Abdo Hezam (LIKAT), and Armin Springer (EMZ Rostock) for fruitful discussions and additional investigations.

**Conflicts of Interest:** The authors declare no conflict of interest.

## References

1. Kumar, A.; Khan, M.; He, J.; Lo, I.M.C. Recent developments and challenges in practical application of visible light driven TiO<sub>2</sub>-based heterojunctions for PPCP degradation: A critical review. *Water Res.* **2020**, *170*, 115356. [[CrossRef](#)] [[PubMed](#)]
2. Liu, J.-L.; Wong, M.-H. Pharmaceuticals and personal care products (PPCPs): A review on environmental contamination in China. *Environ. Int.* **2013**, *59*, 208–224. [[CrossRef](#)]
3. Xu, W.; Zhang, G.; Li, X.; Zou, S.; Li, P.; Hu, Z.; Li, J. Occurrence and elimination of antibiotics at four sewage treatment plants in the Pearl River Delta (PRD), South China. *Water Res.* **2007**, *41*, 4526–4534. [[CrossRef](#)]
4. Kumar, A.; Khan, M.; Fang, L.; Lo, I.M.C. Visible light driven N-TiO<sub>2</sub>@SiO<sub>2</sub>@Fe<sub>3</sub>O<sub>4</sub> magnetic nanophotocatalysts: Synthesis, characterization, and photocatalytic degradation of PPCPs. *J. Hazard. Mater.* **2019**, *370*, 108–116. [[CrossRef](#)] [[PubMed](#)]
5. Fung, C.S.L.; Khan, M.; Kumar, A.; Lo, I.M.C. Visible-light-driven photocatalytic removal of PPCPs using magnetically separable bismuth oxybromo-iodide solid solutions: Mechanisms, pathways, and reusability in real sewage. *Sep. Purif. Technol.* **2019**, *216*, 102–114. [[CrossRef](#)]
6. Khan, M.; Fung, C.S.L.; Kumar, A.; Lo, I.M.C. Magnetically separable BiOBr/Fe<sub>3</sub>O<sub>4</sub>@SiO<sub>2</sub> for visible-light-driven photocatalytic degradation of ibuprofen: Mechanistic investigation and prototype development. *J. Hazard. Mater.* **2019**, *365*, 733–743. [[CrossRef](#)]
7. Fisher, M.; Arbuckle, T.E.; MacPherson, S.; Braun, J.M.; Feeley, M.; Gaudreau, É. Phthalate and BPA Exposure in Women and Newborns through Personal Care Product Use and Food Packaging. *Environ. Sci. Technol.* **2019**, *53*, 10813–10826. [[CrossRef](#)]
8. Cantonwine, D.E.; Cordero, J.F.; Rivera-González, L.O.; Anzalota Del Toro, L.V.; Ferguson, K.K.; Mukherjee, B.; Calafat, A.M.; Crespo, N.; Jiménez-Vélez, B.; Padilla, I.Y.; et al. Urinary phthalate metabolite concentrations among pregnant women in Northern Puerto Rico: Distribution, temporal variability, and predictors. *Environ. Int.* **2014**, *62*, 1–11. [[CrossRef](#)]
9. Liu, R.; Mabury, S.A. Synthetic phenolic antioxidants in personal care products in Toronto, Canada: Occurrence, human exposure, and discharge via greywater. *Environ. Sci. Technol.* **2019**, *53*, 13440–13448. [[CrossRef](#)]
10. Bonnefille, B.; Gomez, E.; Alali, M.; Rosain, D.; Fenet, H.; Courant, F. Metabolomics assessment of the effects of diclofenac exposure on *Mytilus galloprovincialis*: Potential effects on osmoregulation and reproduction. *Sci. Total Environ.* **2018**, *613–614*, 611–618. [[CrossRef](#)]
11. Wang, C.; Yang, L.; Wang, S.; Zhang, Z.; Yu, Y.; Wang, M.; Cromie, M.; Gao, W.; Wang, S.-L. The classic EDCs, phthalate esters and organochlorines, in relation to abnormal sperm quality: A systematic review with meta-analysis. *Sci. Rep.* **2016**, *6*, 19982. [[CrossRef](#)]
12. Ferguson, K.K.; Chen, Y.-H.; VanderWeele, T.J.; McElrath, T.F.; Meeker, J.D.; Mukherjee, B. Mediation of the Relationship between Maternal Phthalate Exposure and Preterm Birth by Oxidative Stress with Repeated Measurements across Pregnancy. *Environ. Health Perspect.* **2017**, *125*, 488–494. [[CrossRef](#)] [[PubMed](#)]
13. Werner, E.F.; Braun, J.M.; Yolton, K.; Khoury, J.C.; Lanphear, B.P. The association between maternal urinary phthalate concentrations and blood pressure in pregnancy: The HOME Study. *Environ. Health* **2015**, *14*, 75. [[CrossRef](#)]
14. Lien, Y.-J.; Ku, H.-Y.; Su, P.-H.; Chen, S.-J.; Chen, H.-Y.; Liao, P.-C.; Chen, W.-J.; Wang, S.-L. Prenatal Exposure to Phthalate Esters and Behavioral Syndromes in Children at 8 Years of Age: Taiwan Maternal and Infant Cohort Study. *Environ. Health Perspect.* **2015**, *123*, 95–100. [[CrossRef](#)] [[PubMed](#)]
15. Benjamin, S.; Masai, E.; Kamimura, N.; Takahashi, K.; Anderson, R.C.; Faisal, P.A. Phthalates impact human health: Epidemiological evidences and plausible mechanism of action. *J. Hazard. Mater.* **2017**, *340*, 360–383. [[CrossRef](#)] [[PubMed](#)]
16. Adibi, J.J.; Lee, M.K.; Naimi, A.I.; Barrett, E.; Nguyen, R.H.; Sathyanarayana, S.; Zhao, Y.; Thiet, M.-P.; Redmon, J.B.; Swan, S.H. Human Chorionic Gonadotropin Partially Mediates Phthalate Association With Male and Female Anogenital Distance. *J. Clin. Endocrinol. Metab.* **2015**, *100*, E1216–E1224. [[CrossRef](#)]
17. Swan, S.H.; Sathyanarayana, S.; Barrett, E.S.; Janssen, S.; Liu, F.; Nguyen, R.H.N.; Redmon, J.B.; TIDES Study Team. First trimester phthalate exposure and anogenital distance in newborns. *Hum. Reprod.* **2015**, *30*, 963–972. [[CrossRef](#)]
18. Gascon, M.; Casas, M.; Morales, E.; Valvi, D.; Ballesteros-Gómez, A.; Luque, N.; Rubio, S.; Monfort, N.; Ventura, R.; Martínez, D.; et al. Prenatal exposure to bisphenol A and phthalates and childhood respiratory tract infections and allergy. *J. Allergy Clin. Immunol.* **2015**, *135*, 370–378.e7. [[CrossRef](#)]
19. Segner, H. Moving beyond a descriptive aquatic toxicology: The value of biological process and trait information. *Aquat. Toxicol.* **2011**, *105*, 50–55. [[CrossRef](#)]
20. Gaw, S.; Thomas, K.V.; Hutchinson, T.H. Sources, impacts and trends of pharmaceuticals in the marine and coastal environment. *Philos. Trans. R. Soc. B Biol. Sci.* **2014**, *369*, 20130572. [[CrossRef](#)]
21. He, B.-S.; Wang, J.; Liu, J.; Hu, X.-M. Eco-pharmacovigilance of non-steroidal anti-inflammatory drugs: Necessity and opportunities. *Chemosphere* **2017**, *181*, 178–189. [[CrossRef](#)] [[PubMed](#)]

22. Huang, B.; Lei, C.; Wei, C.; Zeng, G. Chlorinated volatile organic compounds (Cl-VOCs) in environment—Sources, potential human health impacts, and current remediation technologies. *Environ. Int.* **2014**, *71*, 118–138. [[CrossRef](#)] [[PubMed](#)]
23. Bhadra, B.N.; Ahmed, I.; Kim, S.; Jhung, S.H. Adsorptive removal of ibuprofen and diclofenac from water using metal-organic framework-derived porous carbon. *Chem. Eng. J.* **2017**, *314*, 50–58. [[CrossRef](#)]
24. You, Q.; Zhang, Q.; Gu, M.; Du, R.; Chen, P.; Huang, J.; Wang, Y.; Deng, S.; Yu, G. Self-assembled graphitic carbon nitride regulated by carbon quantum dots with optimized electronic band structure for enhanced photocatalytic degradation of diclofenac. *Chem. Eng. J.* **2022**, *431*, 133927. [[CrossRef](#)]
25. Shojaeimehr, T.; Tasbihi, M.; Acharjya, A.; Thomas, A.; Schomäcker, R.; Schwarze, M. Impact of operating conditions for the continuous-flow degradation of diclofenac with immobilized carbon nitride photocatalysts. *J. Photochem. Photobiol. A Chem.* **2020**, *388*, 112182. [[CrossRef](#)]
26. Bi, L.; Chen, Z.; Li, L.; Kang, J.; Zhao, S.; Wang, B.; Yan, P.; Li, Y.; Zhang, X.; Shen, J. Selective adsorption and enhanced photodegradation of diclofenac in water by molecularly imprinted TiO<sub>2</sub>. *J. Hazard. Mater.* **2021**, *407*, 124759. [[CrossRef](#)]
27. Kumar, A.; Khan, M.; He, J.; Lo, I.M.C. Visible-light-driven magnetically recyclable terephthalic acid functionalized g-C<sub>3</sub>N<sub>4</sub>/TiO<sub>2</sub> heterojunction nanophotocatalyst for enhanced degradation of PPCPs. *Appl. Catal. B Environ.* **2020**, *270*, 118898. [[CrossRef](#)]
28. Moreira, N.F.F.; Orge, C.A.; Ribeiro, A.R.; Faria, J.L.; Nunes, O.C.; Pereira, M.F.R.; Silva, A.M.T. Fast mineralization and detoxification of amoxicillin and diclofenac by photocatalytic ozonation and application to an urban wastewater. *Water Res.* **2015**, *87*, 87–96. [[CrossRef](#)]
29. Sun, J.; Guo, Y.; Wang, Y.; Cao, D.; Tian, S.; Xiao, K.; Mao, R.; Zhao, X. H<sub>2</sub>O<sub>2</sub> assisted photoelectrocatalytic degradation of diclofenac sodium at g-C<sub>3</sub>N<sub>4</sub>/BiVO<sub>4</sub> photoanode under visible light irradiation. *Chem. Eng. J.* **2018**, *332*, 312–320. [[CrossRef](#)]
30. Escapa, C.; Torres, T.; Neuparth, T.; Coimbra, R.N.; Garcia, A.I.; Santos, M.M.; Otero, M. Zebrafish embryo bioassays for a comprehensive evaluation of microalgae efficiency in the removal of diclofenac from water. *Sci. Total Environ.* **2018**, *640–641*, 1024–1033. [[CrossRef](#)]
31. Yang, Y.; Li, X.; Zhou, C.; Xiong, W.; Zeng, G.; Huang, D.; Zhang, C.; Wang, W.; Song, B.; Tang, X.; et al. Recent advances in application of graphitic carbon nitride-based catalysts for degrading organic contaminants in water through advanced oxidation processes beyond photocatalysis: A critical review. *Water Res.* **2020**, *184*, 116200. [[CrossRef](#)] [[PubMed](#)]
32. Verlicchi, P.; Al Aukidy, M.; Zambello, E. Occurrence of pharmaceutical compounds in urban wastewater: Removal, mass load and environmental risk after a secondary treatment—A review. *Sci. Total Environ.* **2012**, *429*, 123–155. [[CrossRef](#)] [[PubMed](#)]
33. Kumar, A.; Khan, M.; Zeng, X.; Lo, I.M.C. Development of g-C<sub>3</sub>N<sub>4</sub>/TiO<sub>2</sub>/Fe<sub>3</sub>O<sub>4</sub>@SiO<sub>2</sub> heterojunction via sol-gel route: A magnetically recyclable direct contact Z-scheme nanophotocatalyst for enhanced photocatalytic removal of ibuprofen from real sewage effluent under visible light. *Chem. Eng. J.* **2018**, *353*, 645–656. [[CrossRef](#)]
34. Wang, J.; Wang, S. Removal of pharmaceuticals and personal care products (PPCPs) from wastewater: A review. *J. Environ. Manag.* **2016**, *182*, 620–640. [[CrossRef](#)] [[PubMed](#)]
35. Ye, S.; Yan, M.; Tan, X.; Liang, J.; Zeng, G.; Wu, H.; Song, B.; Zhou, C.; Yang, Y.; Wang, H. Facile assembled biochar-based nanocomposite with improved graphitization for efficient photocatalytic activity driven by visible light. *Appl. Catal. B Environ.* **2019**, *250*, 78–88. [[CrossRef](#)]
36. Pirhashemi, M.; Habibi-Yangjeh, A.; Rahim Pouran, S. Review on the criteria anticipated for the fabrication of highly efficient ZnO-based visible-light-driven photocatalysts. *J. Ind. Eng. Chem.* **2018**, *62*, 1–25. [[CrossRef](#)]
37. Farooq, N.; Luque, R.; Hessien, M.M.; Qureshi, A.M.; Sahiba, F.; Nazir, M.A.; ur Rehman, A. A Comparative Study of Cerium- and Ytterbium-Based GO/g-C<sub>3</sub>N<sub>4</sub>/Fe<sub>2</sub>O<sub>3</sub> Composites for Electrochemical and Photocatalytic Applications. *Appl. Sci.* **2021**, *11*, 9000. [[CrossRef](#)]
38. Chen, Z.; Zhang, S.; Liu, Y.; Alharbi, N.S.; Rabah, S.O.; Wang, S.; Wang, X. Synthesis and fabrication of g-C<sub>3</sub>N<sub>4</sub>-based materials and their application in elimination of pollutants. *Sci. Total Environ.* **2020**, *731*, 139054. [[CrossRef](#)]
39. Kang, J.; Jin, C.; Li, Z.; Wang, M.; Chen, Z.; Wang, Y. Dual Z-scheme MoS<sub>2</sub>/g-C<sub>3</sub>N<sub>4</sub>/Bi<sub>24</sub>O<sub>31</sub>Cl<sub>10</sub> ternary heterojunction photocatalysts for enhanced visible-light photodegradation of antibiotic. *J. Alloys Compd.* **2020**, *825*, 153975. [[CrossRef](#)]
40. Xu, J.; Gao, Q.; Wang, Z.; Zhu, Y. An all-organic 0D/2D supramolecular porphyrin/g-C<sub>3</sub>N<sub>4</sub> heterojunction assembled via π-π interaction for efficient visible photocatalytic oxidation. *Appl. Catal. B Environ.* **2021**, *291*, 120059. [[CrossRef](#)]
41. Li, W.; Chu, X.-S.; Wang, F.; Dang, Y.-Y.; Liu, X.-Y.; Wang, X.-C.; Wang, C.-Y. Enhanced cocatalyst-support interaction and promoted electron transfer of 3D porous g-C<sub>3</sub>N<sub>4</sub>/GO-M (Au, Pd, Pt) composite catalysts for hydrogen evolution. *Appl. Catal. B Environ.* **2021**, *288*, 120034. [[CrossRef](#)]
42. Xing, W.; Tu, W.; Han, Z.; Hu, Y.; Meng, Q.; Chen, G. Template-Induced High-Crystalline g-C<sub>3</sub>N<sub>4</sub> Nanosheets for Enhanced Photocatalytic H<sub>2</sub> Evolution. *ACS Energy Lett.* **2018**, *3*, 514–519. [[CrossRef](#)]
43. Kumar, O.P.; Shahzad, K.; Nazir, M.A.; Farooq, N.; Malik, M.; Ahmad Shah, S.S.; Rehman, A. Photo-Fenton activated C<sub>3</sub>N<sub>4</sub><sub>x</sub>/AgO<sub>y</sub>@Co<sub>1-x</sub>Bi<sub>0.1-y</sub>O<sub>7</sub> dual s-scheme heterojunction towards degradation of organic pollutants. *Opt. Mater.* **2022**, *126*, 112199. [[CrossRef](#)]
44. Zhang, W.; Zhou, L.; Shi, J.; Deng, H. Synthesis of Ag<sub>3</sub>PO<sub>4</sub>/g-C<sub>3</sub>N<sub>4</sub> Composite with Enhanced Photocatalytic Performance for the Photodegradation of Diclofenac under Visible Light Irradiation. *Catalysts* **2018**, *8*, 45. [[CrossRef](#)]
45. Yan, Y.; Yang, Q.; Shang, Q.; Ai, J.; Yang, X.; Wang, D.; Liao, G. Ru doped graphitic carbon nitride mediated peroxymonosulfate activation for diclofenac degradation via singlet oxygen. *Chem. Eng. J.* **2022**, *430*, 133174. [[CrossRef](#)]

46. Oliveros, A.N.; Pimentel, J.A.I.; de Luna, M.D.G.; Garcia-Segura, S.; Abarca, R.R.M.; Doong, R.-A. Visible-light photocatalytic diclofenac removal by tunable vanadium pentoxide/boron-doped graphitic carbon nitride composite. *Chem. Eng. J.* **2021**, *403*, 126213. [[CrossRef](#)]
47. Ong, W.J.; Tan, L.L.; Ng, Y.H.; Yong, S.T.; Chai, S.P. Graphitic Carbon Nitride (g-C<sub>3</sub>N<sub>4</sub>)-Based Photocatalysts for Artificial Photosynthesis and Environmental Remediation: Are We a Step Closer To Achieving Sustainability? *Chem. Rev.* **2016**, *116*, 7159–7329. [[CrossRef](#)]
48. Huang, S.; Zhang, Q.; Liu, P.; Ma, S.; Xie, B.; Yang, K.; Zhao, Y. Novel up-conversion carbon quantum dots/ $\alpha$ -FeOOH nanohybrids eliminate tetracycline and its related drug resistance in visible-light responsive Fenton system. *Appl. Catal. B Environ.* **2020**, *263*, 118336. [[CrossRef](#)]
49. Wang, F.; Chen, P.; Feng, Y.; Xie, Z.; Liu, Y.; Su, Y.; Zhang, Q.; Wang, Y.; Yao, K.; Lv, W.; et al. Facile synthesis of N-doped carbon dots/g-C<sub>3</sub>N<sub>4</sub> photocatalyst with enhanced visible-light photocatalytic activity for the degradation of indomethacin. *Appl. Catal. B Environ.* **2017**, *207*, 103–113. [[CrossRef](#)]
50. Liu, W.; Li, Y.; Liu, F.; Jiang, W.; Zhang, D.; Liang, J. Visible-light-driven photocatalytic degradation of diclofenac by carbon quantum dots modified porous g-C<sub>3</sub>N<sub>4</sub>: Mechanisms, degradation pathway and DFT calculation. *Water Res.* **2019**, *151*, 8–19. [[CrossRef](#)]
51. Korah, B.K.; Chacko, A.R.; Abraham, T.; Mathew, B. Recent Progress and Future Perspectives of Carbon Dots in the Detection, Degradation, and Enhancement of Drugs. *Part. Part. Syst. Charact.* **2022**, *39*, 2100264. [[CrossRef](#)]
52. Seng, R.X.; Tan, L.-L.; Lee, W.P.C.; Ong, W.-J.; Chai, S.-P. Nitrogen-doped carbon quantum dots-decorated 2D graphitic carbon nitride as a promising photocatalyst for environmental remediation: A study on the importance of hybridization approach. *J. Environ. Manag.* **2020**, *255*, 109936. [[CrossRef](#)] [[PubMed](#)]
53. Liu, X.; Li, F.; Liu, Y.; Li, P.; Chen, L.; Li, B.; Qian, T.; Liu, W. Degradation of diclofenac in a photosensitization-like photocatalysis process using palladium quantum dots deposited graphite carbon nitride under solar light. *J. Environ. Chem. Eng.* **2022**, *10*, 107545. [[CrossRef](#)]
54. Wang, H.-X.; Xiao, J.; Yang, Z.; Tang, H.; Zhu, Z.-T.; Zhao, M.; Liu, Y.; Zhang, C.; Zhang, H.-L. Rational design of nitrogen and sulfur co-doped carbon dots for efficient photoelectrical conversion applications. *J. Mater. Chem. A* **2015**, *3*, 11287–11293. [[CrossRef](#)]
55. Bai, L.; Liu, L.; Pang, J.; Chen, Z.; Wei, M.; Wu, Y.; Dong, G.; Zhang, J.; Shan, D.; Wang, B. N,P-codoped carbon quantum dots-decorated TiO<sub>2</sub> nanowires as nanosized heterojunction photocatalyst with improved photocatalytic performance for methyl blue degradation. *Environ. Sci. Pollut. Res.* **2021**, *29*, 9932–9943. [[CrossRef](#)]
56. Chava, R.K.; Im, Y.; Kang, M. Nitrogen doped carbon quantum dots as a green luminescent sensitizer to functionalize ZnO nanoparticles for enhanced photovoltaic conversion devices. *Mater. Res. Bull.* **2017**, *94*, 399–407. [[CrossRef](#)]
57. Li, X.; Shi, H.; Yan, X.; Zuo, S.; Zhang, Y.; Wang, T.; Luo, S.; Yao, C.; Ni, C. Palygorskite Immobilized Direct Z-Scheme Nitrogen-Doped Carbon Quantum dots/PrFeO<sub>3</sub> for Photo-SCR Removal of NO<sub>x</sub>. *ACS Sustain. Chem. Eng.* **2018**, *6*, 10616–10627. [[CrossRef](#)]
58. Zhang, J.; Zhang, X.; Dong, S.; Zhou, X.; Dong, S. N-doped carbon quantum dots/TiO<sub>2</sub> hybrid composites with enhanced visible light driven photocatalytic activity toward dye wastewater degradation and mechanism insight. *J. Photochem. Photobiol. A Chem.* **2016**, *325*, 104–110. [[CrossRef](#)]
59. Zhang, H.; Zhao, L.; Geng, F.; Guo, L.-H.; Wan, B.; Yang, Y. Carbon dots decorated graphitic carbon nitride as an efficient metal-free photocatalyst for phenol degradation. *Appl. Catal. B Environ.* **2016**, *180*, 656–662. [[CrossRef](#)]
60. Xiao, H.; Wang, W.; Liu, G.; Chen, Z.; Lv, K.; Zhu, J. Photocatalytic performances of g-C<sub>3</sub>N<sub>4</sub> based catalysts for RhB degradation: Effect of preparation conditions. *Appl. Surf. Sci.* **2015**, *358*, 313–318. [[CrossRef](#)]
61. Wang, Y.; Bai, X.; Qin, H.; Wang, F.; Li, Y.; Li, X.; Kang, S.; Zuo, Y.; Cui, L. Facile One-Step Synthesis of Hybrid Graphitic Carbon Nitride and Carbon Composites as High-Performance Catalysts for CO<sub>2</sub> Photocatalytic Conversion. *ACS Appl. Mater. Interfaces* **2016**, *8*, 17212–17219. [[CrossRef](#)] [[PubMed](#)]
62. Muhmood, T.; Uddin, A. Fabrication of spherical-graphitic carbon nitride via hydrothermal method for enhanced photo-degradation ability towards antibiotic. *Chem. Phys. Lett.* **2020**, *753*, 137604. [[CrossRef](#)]
63. Wang, X.; Li, Q.; Gan, L.; Ji, X.; Chen, F.; Peng, X.; Zhang, R. 3D macropore carbon-vacancy g-C<sub>3</sub>N<sub>4</sub> constructed using polymethylmethacrylate spheres for enhanced photocatalytic H<sub>2</sub> evolution and CO<sub>2</sub> reduction. *J. Energy Chem.* **2021**, *53*, 139–146. [[CrossRef](#)]
64. Guo, M.; Liu, W.; Huang, J.; Liu, J.; Yin, S.; Leng, J. Enhanced crystal quality of perovskite via protonated graphitic carbon nitride added in carbon-based perovskite solar cells. *Chin. J. Chem. Phys.* **2022**, *35*, 390–398. [[CrossRef](#)]
65. Ong, W.-J.; Putri, L.K.; Tan, Y.-C.; Tan, L.-L.; Li, N.; Ng, Y.H.; Wen, X.; Chai, S.-P. Unravelling charge carrier dynamics in protonated g-C<sub>3</sub>N<sub>4</sub> interfaced with carbon nanodots as co-catalysts toward enhanced photocatalytic CO<sub>2</sub> reduction: A combined experimental and first-principles DFT study. *Nano Res.* **2017**, *10*, 1673–1696. [[CrossRef](#)]
66. Hou, H.; Banks, C.E.; Jing, M.; Zhang, Y.; Ji, X. Carbon Quantum Dots and Their Derivative 3D Porous Carbon Frameworks for Sodium-Ion Batteries with Ultralong Cycle Life. *Adv. Mater.* **2015**, *27*, 7861–7866. [[CrossRef](#)]
67. Enli, L. Rational copolymerization strategy engineered C self-doped g-C<sub>3</sub>N<sub>4</sub> for efficient and robust solar photocatalytic H<sub>2</sub> evolution. *Renew. Energy* **2021**, *178*, 757–765. [[CrossRef](#)]

68. Wang, C.; Fan, H.; Ren, X.; Fang, J.; Ma, J.; Zhao, N. Porous graphitic carbon nitride nanosheets by pre-polymerization for enhanced photocatalysis. *Mater. Charact.* **2018**, *139*, 89–99. [[CrossRef](#)]
69. Jiao, Y.; Li, Y.; Wang, J.; He, Z.; Li, Z.-J. Exfoliation-induced exposure of active sites for g-C<sub>3</sub>N<sub>4</sub>/N-doped carbon dots heterojunction to improve hydrogen evolution activity. *Mol. Catal.* **2020**, *497*, 111223. [[CrossRef](#)]
70. Han, C.; Li, J.; Ma, Z.; Xie, H.; Waterhouse, G.I.N.; Ye, L.; Zhang, T. Black phosphorus quantum dot/g-C<sub>3</sub>N<sub>4</sub> composites for enhanced CO<sub>2</sub> photoreduction to CO. *Sci. China Mater.* **2018**, *61*, 1159–1166. [[CrossRef](#)]
71. Jamshaid, M.; Nazir, M.A.; Najam, T.; Shah, S.S.A.; Khan, H.M.; Rehman, A.U. Facile synthesis of Yb<sup>3+</sup>-Zn<sup>2+</sup> substituted M type hexaferrites: Structural, electric and photocatalytic properties under visible light for methylene blue removal. *Chem. Phys. Lett.* **2022**, *805*, 139939. [[CrossRef](#)]
72. Shi, L.; Chang, K.; Huabin, Z.; Hai, X.; Yang, L.; Wang, T.; Ye, J. Drastic Enhancement of Photocatalytic Activities over Phosphoric Acid Protonated Porous g-C<sub>3</sub>N<sub>4</sub> Nanosheets under Visible Light. *Small* **2016**, *12*, 4431–4439. [[CrossRef](#)] [[PubMed](#)]
73. Ong, W.-J.; Tan, L.-L.; Chai, S.-P.; Yong, S.-T.; Mohamed, A.R. Surface charge modification via protonation of graphitic carbon nitride (g-C<sub>3</sub>N<sub>4</sub>) for electrostatic self-assembly construction of 2D/2D reduced graphene oxide (rGO)/g-C<sub>3</sub>N<sub>4</sub> nanostructures toward enhanced photocatalytic reduction of carbon dioxide to methane. *Nano Energy* **2015**, *13*, 757–770. [[CrossRef](#)]
74. Wang, Z.; Guan, W.; Sun, Y.; Dong, F.; Zhou, Y.; Ho, W.K. Water-assisted production of honeycomb-like g-C<sub>3</sub>N<sub>4</sub> with ultralong carrier lifetime and outstanding photocatalytic activity. *Nanoscale* **2015**, *7*, 2471–2479. [[CrossRef](#)] [[PubMed](#)]
75. Qin, H.; Guo, R.-T.; Liu, X.-Y.; Shi, X.; Wang, Z.-Y.; Tang, J.-Y.; Pan, W.-G. 0D NiS<sub>2</sub> quantum dots modified 2D g-C<sub>3</sub>N<sub>4</sub> for efficient photocatalytic CO<sub>2</sub> reduction. *Colloids Surf. A Physicochem. Eng. Asp.* **2020**, *600*, 124912. [[CrossRef](#)]
76. Li, K.; Su, F.-Y.; Zhang, W.-D. Modification of g-C<sub>3</sub>N<sub>4</sub> nanosheets by carbon quantum dots for highly efficient photocatalytic generation of hydrogen. *Appl. Surf. Sci.* **2016**, *375*, 110–117. [[CrossRef](#)]
77. Zhang, Z.; Lin, S.; Li, X.; Li, H.; Cui, W. Metal free and efficient photoelectrocatalytic removal of organic contaminants over g-C<sub>3</sub>N<sub>4</sub> nanosheet films decorated with carbon quantum dots. *RSC Adv.* **2017**, *7*, 56335–56343. [[CrossRef](#)]
78. Phang, S.J.; Tan, L.-L. Recent advances in carbon quantum dot (CQD)-based two dimensional materials for photocatalytic applications. *Catal. Sci. Technol.* **2019**, *9*, 5882–5905. [[CrossRef](#)]
79. Leelavathi, A.; Madras, G.; Ravishankar, N. New Insights into Electronic and Geometric Effects in the Enhanced Photoelectrooxidation of Ethanol Using ZnO Nanorod/Ultrathin Au Nanowire Hybrids. *J. Am. Chem. Soc.* **2014**, *136*, 14445–14455. [[CrossRef](#)]
80. Achilleos, A.; Hapeshi, E.; Xekoukoulotakis, N.P.; Mantzavinos, D.; Fatta-Kassinos, D. Factors affecting diclofenac decomposition in water by UV-A/TiO<sub>2</sub> photocatalysis. *Chem. Eng. J.* **2010**, *161*, 53–59. [[CrossRef](#)]
81. Méndez-Arriaga, F.; Esplugas, S.; Giménez, J. Photocatalytic degradation of non-steroidal anti-inflammatory drugs with TiO<sub>2</sub> and simulated solar irradiation. *Water Res.* **2008**, *42*, 585–594. [[CrossRef](#)] [[PubMed](#)]
82. Zhu, S.; Li, X.; Kang, J.; Duan, X.; Wang, S. Persulfate Activation on Crystallographic Manganese Oxides: Mechanism of Singlet Oxygen Evolution for Nonradical Selective Degradation of Aqueous Contaminants. *Environ. Sci. Technol.* **2019**, *53*, 307–315. [[CrossRef](#)] [[PubMed](#)]
83. Wang, J.; Wang, S. Reactive species in advanced oxidation processes: Formation, identification and reaction mechanism. *Chem. Eng. J.* **2020**, *401*, 126158. [[CrossRef](#)]
84. Guo, Y.; Li, Y.; Zhu, T.; Ye, M. Effects of Concentration and Adsorption Product on the Adsorption of SO<sub>2</sub> and NO on Activated Carbon. *Energy Fuels* **2013**, *27*, 360–366. [[CrossRef](#)]
85. Wang, Y.-D.; Lee, T.-W.; Lo, Y.-C.; Hong, W.-J.; Chen, C. Insights into photochemical stability of graphitic carbon nitride-based photocatalysts in water treatment. *Carbon* **2021**, *175*, 223–232. [[CrossRef](#)]
86. Martin, D.J.; Qiu, K.; Shevlin, S.A.; Handoko, A.D.; Chen, X.; Guo, Z.; Tang, J. Highly Efficient Photocatalytic H<sub>2</sub> Evolution from Water using Visible Light and Structure-Controlled Graphitic Carbon Nitride. *Angew. Chem. Int. Ed.* **2014**, *53*, 9240–9245. [[CrossRef](#)]

**Disclaimer/Publisher’s Note:** The statements, opinions and data contained in all publications are solely those of the individual author(s) and contributor(s) and not of MDPI and/or the editor(s). MDPI and/or the editor(s) disclaim responsibility for any injury to people or property resulting from any ideas, methods, instructions or products referred to in the content.